Seaglider surveys at Ocean Station Papa: Diagnosis of upper-ocean heat and salt balances using least squares with inequality constraints

Noel A. Pelland[1,2] 🆔, Charles C. Eriksen[1], and Meghan F. Cronin[3] 🆔

[1]School of Oceanography, University of Washington, Seattle, Washington, USA, [2]Now at Alaska Fisheries Science Center, NOAA, and Joint Institute for the Study of the Atmosphere and Ocean, University of Washington, Seattle, Washington, USA, [3]Pacific Marine Environmental Laboratory, NOAA, Seattle, Washington, USA

Abstract Heat and salt balances in the upper 200 m are examined using data from Seaglider spatial surveys June 2008 to January 2010 surrounding a NOAA surface mooring at Ocean Station Papa (OSP; 50°N, 145°W). A least-squares approach is applied to repeat Seaglider survey and moored measurements to solve for unknown or uncertain monthly three-dimensional circulation and vertical diffusivity. Within the surface boundary layer, the estimated heat and salt balances are dominated throughout the surveys by turbulent flux, vertical advection, and for heat, radiative absorption. When vertically integrated balances are considered, an estimated upwelling of cool water balances the net surface input of heat, while the corresponding large import of salt across the halocline due to upwelling and diffusion is balanced by surface moisture input and horizontal import of fresh water. Measurement of horizontal gradients allows the estimation of unresolved vertical terms over more than one annual cycle; diffusivity in the upper-ocean transition layer decreases rapidly to the depth of the maximum near-surface stratification in all months, with weak seasonal modulation in the rate of decrease and profile amplitude. Vertical velocity is estimated to be on average upward but with important monthly variations. Results support and expand existing evidence concerning the importance of horizontal advection in the balances of heat and salt in the Gulf of Alaska, highlight time and depth variability in difficult-to-measure vertical transports in the upper ocean, and suggest avenues of further study in future observational work at OSP.

1. Introduction

Ocean Station Papa (OSP; 50°N, 145°W) in the southern Gulf of Alaska (GOA) has been an important site for the study of ocean-atmosphere exchange due to weak background flows that give rise to oceanic balances of heat and freshwater that are often dominated for short periods by local storage and input from or removal to the atmosphere [*Gill and Niiler*, 1973; *Denman and Miyake*, 1973]. However, over an annual cycle, the southern GOA including OSP is a region of net transfer of heat and freshwater from the atmosphere to the ocean [*Large*, 1996; *Moisan and Niiler*, 1998; *Ren and Riser*, 2009; *Schanze et al.*, 2010]. The rates of transfer greatly exceed the observed long-term storage of these quantities in the upper ocean [*Tabata*, 1965; *Freeland et al.*, 1997]. Since there is a difference between surface inputs and local storage over a typical annual cycle at OSP, oceanic advective or diffusive fluxes must be present to close the heat and freshwater budgets.

The mechanisms available to remove heat and freshwater are strongly influenced by upper-ocean stratification at OSP, where a mixed layer and seasonal thermocline overlie a permanent pycnocline, the upper portion of which is dominated by salinity stratification (hereinafter referred to as the "halocline;" Figure 1). The structure of this stratification is such that over a year, any upwelling of cool, deep water that would be large enough to offset the surface heat input would simultaneously increase salinity in disagreement with the observed profiles [*Tabata*, 1965; *Large*, 1996]. This led *Tabata* [1965] and *Large* [1996] to conclude that only weak vertical advection occurs annually which, in concert with vertical diffusion of salt, offsets the surface freshwater input. The net heat input is instead mainly removed by horizontal advection, likely due to seasonal flow acting on seasonal horizontal gradients of temperature in fall and winter, when the climatological ocean cooling is greater than can be explained by the estimated loss of heat to the atmosphere [*Large*, 1996]. This process has been observed in some years [*Tabata*, 1965; *Large et al.*, 1986; *Paduan and deSzoeke*,
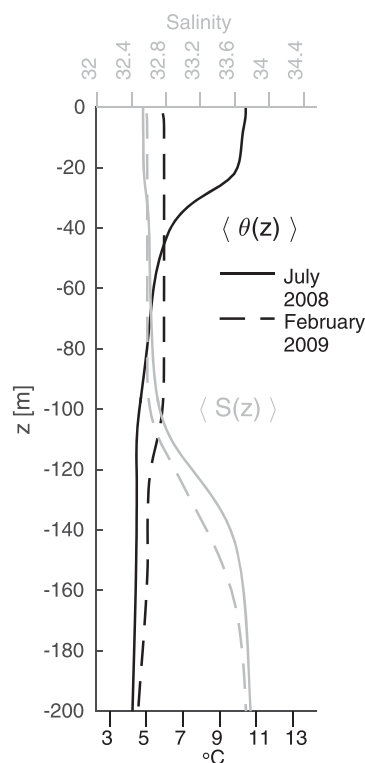
Figure 1. Monthly average vertical profiles of potential temperature θ (black curves) and salinity S (gray curves) from Seaglider surveys at Ocean Station Papa (50°N, 145°W), in July 2008 (solid curves) and February 2009 (dashed). Horizontal axes for θ (S) are scaled by the thermal expansion (haline contraction) coefficient appropriate for average conditions at the surface; i.e., curves are scaled according to their contribution to density stratification. Data from *Pelland et al.* [2016].

1986; *Paduan and Niiler*, 1993; *Torruella*, 1995]. Within the annual cycle, turbulent mixing vertically redistributes surface heat and freshwater input, transferring heat from the surface to the thermocline throughout the year, and freshwater to the top of the halocline in winter which strengthens and maintains the salinity stratification there [*Large*, 1996; *Cronin et al.*, 2015].

While the above description of the annual cycle is a useful conceptual tool, historical records and modern autonomous sampling have demonstrated that perturbations to such a cycle are significant over a variety of time periods, and often arise due to anomalous oceanic fluxes rather than changes in surface inputs [*Large*, 1996; *Jackson et al.*, 2006; *Crawford et al.*, 2007]. Processes that have been cited as possible sources for these ocean fluxes include shifts in orientation of the eastward-flowing North Pacific Current that passes near OSP, alterations in patterns of atmospheric forcing of the GOA gyre, or passing mesoscale eddies [*Freeland and Cummins*, 2005; *Jackson et al.*, 2006; *Crawford et al.*, 2007]. It remains to account for and specifically diagnose the horizontal or vertical fluxes of heat or salt that close these imbalances through direct in situ measurements.

From June 2008 to January 2010, Seaglider autonomous underwater vehicles were deployed at OSP to perform spatial surveys surrounding a National Oceanic and Atmospheric Administration (NOAA) Ocean Climate Stations (OCS) mooring [*Pelland et al.*, 2016, hereinafter PEC1]. These surveys provided continuous estimates of small-scale spatial gradients, at depths up to 1000 m, over more than one annual cycle, a combination not previously achieved in the OSP observational record. Here, we use results from these surveys and moored measurements to diagnose the heat and salt balances in the upper ocean at monthly time scales, including the effects of horizontal and vertical advection, and vertical turbulent diffusion.

In PEC1, Seaglider spatial survey results were used to estimate the horizontal gradients of temperature and salinity, along with vertical profiles of geostrophic velocity, over monthly intervals, revealing anomalous currents and gradients that reflected the presence of a mesoscale meander of the North Pacific Current near OSP. In this study, these quantities are used, along with concurrent surface heat and freshwater fluxes, to pose the heat and salt balances in discrete depth bins in the upper 200 m of the water column in each monthly interval. Since the vertical advection and turbulent diffusion terms in these balances were not measured during Seaglider surveys—and the horizontal components of advection have large uncertainties due to errors in both gradients and currents—a least-squares method is used to determine these terms. Specifically, a system of equations is constructed and least-squares solution obtained for the three-dimensional circulation and vertical diffusion necessary to close time-integrated tracer balances, while deviating within reasonable error bounds from initial estimates or physical assumptions and maintaining inequality constraints on vertical diffusivities. This method—least squares with inequality constraints [*Lawson and Hanson*, 1974]—has wide precedent for determining unknown or uncertain velocity and diffusivity components from tracer data in oceanographic or limnologic problems [*Olbers et al.*, 1985; *Hogg*, 1987; *Tziperman and Hecht*, 1988; *Zhang and Hogg*, 1992; *Wunsch*, 1996; *Anokhin et al.*, 2008], including in the OSP area by *Matear* [1993].

Commonly, such an approach of determining transports from tracer data and assumed dynamics is referred to as an "inverse" method [e.g., *Matear*, 1993]. We acknowledge this terminology while making the distinction that the problem considered in this study is overconstrained (has more independent governing equations than unknown quantities), in contrast to the traditional definition of an inverse method in oceanography as applying to an underdetermined system [*Wunsch*, 1978]. In what follows, section 2.1 summarizes the available observations and surface fluxes. Sections 2.2 and 2.3 describe the methodology of the least-squares problem. In section 3, the least-squares estimates of circulation and diffusion are described,

and these estimates are then used to diagnose heat and salt balances in different depth ranges within the upper 200 m during Seaglider surveys at OSP. Section 4 discusses these results, and the identified profiles of vertical velocity and turbulent diffusion, in the context of previous studies. Conclusions and implications for future studies at OSP follow in section 5.

2. Data and Methods

2.1. Measurements and Surface Fluxes

Individual Seagliders [*Eriksen et al.*, 2001] surveyed at OSP from 8 June 2008 to 18 January 2010 in a sequence of three individual deployments. Seaglider (SG) 144 was deployed from 8 June to 30 August 2008, SG120 from 30 August 2008 to 14 June 2009, and SG144 again from 14 June 2009 to 18 January 2010. Sampling strategy and processing methods are described in detail in PEC1 and *Pelland* [2015] and are summarized here. Seagliders performed 1693 dive-climb cycles, collecting 3386 vertical profiles, while sampling temperature, salinity, pressure, dissolved oxygen, fluorescence, and optical backscatter from the surface to 1000 m depth along a 1:3 vertical:horizontal nominal glide slope. Seagliders sampled within a 50 × 50 km box encompassing the NOAA OCS mooring site, repeating a "bowtie"-shaped navigational track every 14.5 days on average. Each repeat consisted of 36–59 (median 43) dive-climb cycles. For each dive-climb cycle, comparison of Seaglider dead-reckoned horizontal displacement to the observed difference between surface positions gave an estimate of 0–1000 m depth-averaged current (DAC).

Seaglider samples of potential temperature θ, salinity S, dissolved oxygen per unit mass of seawater $[O_2]$, and density ρ in the top 200 m were bin-averaged in depth for each profile. Depth bin spacing was 2 m vertically in the top 150 m, and 5 m from 150 to 200 m depth, which is the lower boundary of the vertical domain considered in this study, as will be described below. Horizontal gradients of scalar variables in each bin were estimated over monthly time intervals using multivariable least-squares regression fits to observations as a function of space and time (PEC1). The monthly time interval corresponds to roughly the time required for a glider to make two complete occupations of the transect pattern, and is the finest time scale on which it can be reasonably expected that the Seaglider surveys provide useful estimates of horizontal gradients in the 50 × 50 km box around OSP. Horizontal density gradients were used to estimate monthly geostrophic velocity profiles referenced to DAC estimates, making them absolute. Horizontal θ/S gradients and geostrophic currents estimated in this manner are reported in PEC1.

Additionally, in this study, vertical profiles of θ and S at the center of the Seaglider track pattern were estimated at the temporal boundaries between monthly intervals, for use in evaluating the local rate-of-change within each month. These values were estimated using a form of local regression estimation [*Cleveland and Devlin*, 1988; *Ridgway et al.*, 2002]: a multivariable regression as a function of space and time, of the same form as used to estimate horizontal gradients in PEC1, was fit to observations of θ or S in a depth bin within ±15 days of the beginning and end of each month, and evaluated at the track center location and day of interest. Results of this procedure are shown for selected depths in Figure 2.

When available, we used daily averaged net surface heat and moisture fluxes estimated by *Cronin et al.* [2015] from observations collected by the NOAA OCS mooring deployed at OSP from June 2007 to present. The OCS mooring samples wind speed and direction, air temperature, relative humidity, downwelling short and longwave radiation, rain rate, and barometric pressure. The sampling strategies for these instruments are described by *Cronin et al.* [2013, 2015], while measurement errors are discussed in *Kubota et al.* [2008]. During gaps in the mooring time series, surface heat and moisture flux components were obtained from the Objectively Analyzed air-sea Fluxes for the Global Oceans (OAFLUX) data set [*Yu and Weller*, 2007], the International Satellite Cloud Climatology Project (ISCCP) [*Zhang et al.*, 2004], and the Global Precipitation Climatology Project (GPCP) [*Huffman et al.*, 2001]. Corrections were applied to the ISCCP outgoing longwave radiative and OAFLUX sensible heat flux components, as well as the OAFLUX evaporation and GPCP precipitation, to remove inferred biases relative to the moored data. Details regarding calculation of the components of the surface heat and moisture fluxes are provided in Appendix A.

This study also used wind stress curl estimates derived from the Cross-Calibrated Multi-Platform (CCMP) L3.0 6 hourly 0.25° gridded winds obtained from the Physical Oceanography Distributed Active Archive Center (PODAAC). Climatological temperature and salinity data were obtained from the 2005–2012 1/4° decadal climatology product in the 2013 World Ocean Atlas (WOA) [*Boyer et al.*, 2013].
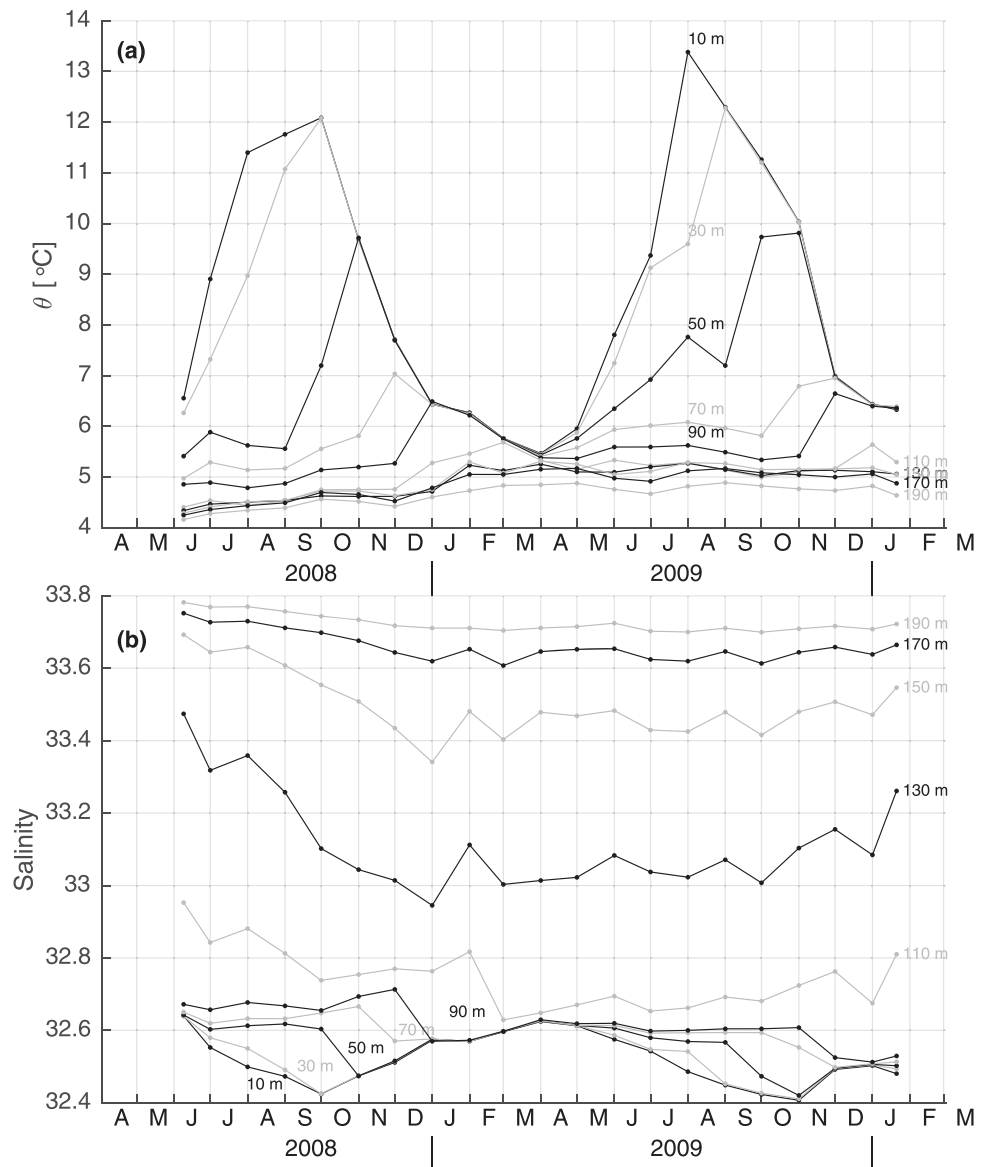
Figure 2. Monthly variation in potential temperature θ (a) and salinity (b) at selected depths during Seaglider surveys at Ocean Station Papa, with alternating black and gray curves to aid visualization. Data represent estimates at center of track pattern obtained via local regression estimation as described in section 2.1.

2.2. Least-Squares Problem Formulation
2.2.1. Governing Equations

Following *Large* [1996], the vertical domain in this study is limited to the upper 200 m, within which the direct influence of surface forcing is reliably confined. The analysis is based on simplified versions of the heat and salt conservation equations appropriate to the upper ocean:

$$\frac{D\theta}{Dt}\left(\equiv \frac{\partial\theta}{\partial t}+u\frac{\partial\theta}{\partial x}+v\frac{\partial\theta}{\partial y}+w\frac{\partial\theta}{\partial z}\right)=-\frac{\partial}{\partial z}\overline{w'\theta'}-\left(\rho_0 c_p\right)^{-1}\frac{\partial}{\partial z}I(z), \tag{1}$$

$$\frac{DS}{Dt}=-\frac{\partial}{\partial z}\overline{w'S'}, \tag{2}$$

where D/Dt is the material derivative, (u, v, w), respectively, indicates the zonal, meridional, and vertical components of velocity, $\overline{w'\theta'}$ $(\overline{w'S'})$ is the vertical turbulent flux of temperature (salinity), and $I(z)$ is the (positive upward) solar radiative heat flux (W m^{-2}). In (1) the volumetric heat capacity has been assumed constant

($\rho_0 c_p \equiv 4.0923 \times 10^6$ J °C^{-1} m^{-3}) and convergence of horizontal turbulent flux has been neglected in both (1) and (2). Surface boundary conditions for the vertical turbulent flux profiles are given by [*Large*, 1996]

$$\overline{w'\theta'}_0 = (\rho_0 c_p)^{-1}(Q_{LW} + Q_L + Q_H), \tag{3}$$

$$\overline{w'S'}_0 = -S_0(E-P), \tag{4}$$

where Q_{LW}, Q_L, and Q_H are, respectively, the longwave, latent, and sensible components of surface heat flux, S_0 is the surface salinity, while E and P are, respectively, the surface evaporation and precipitation (cm d^{-1}). The surface shortwave radiative heat flux Q_S provides the surface boundary condition for $I(z)$, and its decay with depth is assumed to be consistent with Jerlov Type IA water [*Paulson and Simpson*, 1977].

Equations based on the balances (1) and (2), described below, were posed in each of 86 depth bins that span the surface to 200 m depth (section 2.1), and for each of 20 partial or complete calendar months sampled during the Seaglider time series. The approach is to consider the relatively more uncertain quantities in (1) and (2) as unknowns within this system of equations, and to find the set of unknowns that best satisfies these equations, while also deviating as little as possible from initial estimates or a priori expectations. In (1) and (2), estimates of horizontal and vertical gradients and time derivatives of θ and S, as well as horizontal geostrophic velocity are available from Seaglider surveys at monthly intervals (section 2.1, PEC1). The surface boundary conditions (3) and (4) are also well-constrained during Seaglider surveys from monthly averages of the OCS mooring and remote sensing surface fluxes. Collectively, these variables are relatively more certain than the subsurface vertical turbulent fluxes or w, which were not measured during Seaglider surveys at OSP. Comparison of modeled versus observed glider descent and ascent rates allows inference of w from Seaglider profiling for strong variations over short periods [*Frajka-Williams et al.*, 2011; *Beaird et al.*, 2012], but this approach fails on the monthly time scales considered here.

Vertical velocity and turbulent fluxes are treated as unknowns because they were not directly measured during Seaglider surveys. Since estimates of u and v and horizontal gradients are available from PEC1, it would be possible to use these to compute horizontal advection in (1) and (2) and solve the system of equations for only the unknown w and turbulent fluxes. However, using this approach in a similar least-squares problem yielded temporal mean-square residual errors in the tracer equations that exceeded the observed variance in the halocline [*Pelland*, 2015] and unrealistically large-magnitude vertical diffusivity profiles (data not shown). Although estimates of geostrophic currents from PEC1 were shown to be in good qualitative agreement with measurements from two independent platforms, computing advection from these currents involves the product of the currents and horizontal gradients, which each contain error. Both variable types cannot be treated as unknowns in a linear problem, since they appear as a product in the governing equations. For simplicity, we treat only horizontal velocity components as unknowns. This has the advantage that, for each depth bin, there are only two unknown horizontal velocity components, as opposed to four unknown θ and S horizontal gradient components. Note that the term "unknown" is therefore used in a mathematical sense to refer to elements of the least-squares solution that are to be obtained, and that unknowns in this problem in fact include both unmeasured (w and turbulent fluxes) and uncertain (u and v) quantities. Additional equations described below will be added to the problem to constrain the u and v solution elements within a reasonable error bound from the initial estimates obtained in PEC1.

The system of governing equations is based on discretized versions of the time-integrated heat and salt balances in the upper 200 m during Seaglider surveys at OSP. Integrating (1) between a starting time t_s and final time t_f yields

$$\theta(z,t_f) - \theta(z,t_s) + \int_{t_s}^{t_f} \frac{\partial}{\partial z}\left(\frac{I(z,\tau)}{\rho_0 c_p}\right) d\tau =$$

$$\tag{5}$$

$$-\int_{t_s}^{t_f}\left[u(z,\tau)\frac{\partial\theta(z,\tau)}{\partial x} + v(z,\tau)\frac{\partial\theta(z,\tau)}{\partial y} + w(z,\tau)\frac{\partial\theta(z,\tau)}{\partial z}\right] d\tau - \int_{t_s}^{t_f}\frac{\partial}{\partial z}\overline{w'\theta'}(z,\tau) d\tau,$$

where τ represents a dummy variable of integration with respect to time, and the equation has been rearranged from (1) such that all terms containing unknowns (u, v, w, $\overline{w'\theta'}$) are on the right-hand side. The

balance (5) is discretized, in each depth bin, for time integrals that extend from the initiation of the time series to the end of each of 20 monthly intervals as described above. These equations take the form

$$
\theta_{i,M+0.5} - \theta_{i,0.5} + \sum_{j=1}^{M} \Delta t_j (\rho_0 c_p)^{-1} \frac{\partial I}{\partial z}\bigg|_{ij} = -\sum_{j=1}^{M} \Delta t_j \left[u_{ij} \frac{\partial \theta}{\partial x}\bigg|_{ij} + v_{ij} \frac{\partial \theta}{\partial y}\bigg|_{ij} + w_{ij} \frac{\partial \theta}{\partial z}\bigg|_{ij} \right] - \sum_{j=1}^{M} \frac{\Delta t_j}{\Delta z_i} \left[\overline{w'\theta'}\bigg|_{i+0.5,j} - \overline{w'\theta'}\bigg|_{i-0.5,j} \right],
$$

(6)

where subscripts refer to depth bin i and monthly interval j. Partial subscripts refer to quantities evaluated at the bin or interval boundaries; i.e., $\theta_{i,0.5}$ refers to θ in depth bin i at the beginning of the first monthly interval, 8 June 2008 (section 2.1). The variable Δz_i refers to the thickness of bin i, and Δt_j is the duration of interval j.

For each of $N_d = 86$ depth bins i, the balance (6) is used to write 20 equations, each based on summations taken from $j = 1$ to $j = M$, where $M = 1, 2, \ldots, 20$. An additional 20 equations are written for the vertical integral of these balances across the upper 200 m. Similar equations are written for the time-integrated salinity balance, yielding $2M(N_d + 1) = 3480$ tracer equations.

We chose to formulate the system using time-integrated balances of θ and S in order to more fully incorporate the scope of information provided by the persistence of Seaglider surveys over 18 months at OSP; i.e., to approach the problem in a "global" rather than "local" sense. Examination of (6) reveals that the unknowns of a given monthly interval appear in any equation in which the time-integral is taken to the end of that month or later—for example, $u_{i,1}$ appears in all 20 equations at depth i. This would not be the case if the tendency balances (1) and (2) were solved independently in each monthly interval (local approach). Whereas the local approach would find a solution that minimizes the sum of square errors in each monthly interval, the global approach minimizes the sum of squares of the cumulative (in time) errors from the initiation of the time series. Observations of θ or S made at any point after the initiation of the time series provide information about the unknown physical transports at earlier times [*Wunsch*, 1996], and formulating the least-squares problem in terms of the time integral (5) is a way of including this information when determining the solution elements.

2.2.2. Parameterizing the Unknowns

Within the system of tracer equations, there are $2MN_d = 3440$ u and v geostrophic velocity components to be estimated. Monthly average horizontal Ekman velocities are not considered, though the solution is not sensitive to their inclusion, and an alternate solution in which Ekman velocities were specified did not have uniformly smaller tracer residuals [*Pelland*, 2015, see also discussion in section 4.3]. Beyond geostrophic u and v, there are additional unknown vertical velocities and turbulent fluxes. The number of elements of the solution vector related to these quantities was reduced in comparison to u or v by using a series of simplifying assumptions and parameterizations, described next.

First, in each monthly interval, the upper 200 m was partitioned into three layers which are, in order of increasing depth, an unstratified surface layer (SL), a stratified transition layer (TL), and an interior layer (INT). These layers were chosen primarily to reflect the typical vertical structure of upper-ocean turbulence, in which turbulent fluxes are expected to be much larger in the SL and TL than INT [e.g., *Sun et al.*, 2013]. The layers were defined in each month using the monthly average profile of square buoyancy frequency, representative of density stratification absent the effects of compressibility, $N^2 = -g(\alpha \partial \theta / \partial z - \beta \partial S / \partial z)$, where g is gravitational acceleration, and α (β) is the thermal expansion (haline contraction) coefficient as defined in *McDougall* [1984]. The shallowest depth of the TL in each interval was defined as the first depth bin greater than 10 m at which N^2 reaches 10% of its peak value in the average profile from that month. The TL extends from this depth ($z = -h_j$) to the first bin at least 50 m deeper ($z = -H_j$). This value was chosen such that the TL thickness would be great enough to resolve the decrease in turbulent fluxes to background levels in all months; 50 m was the approximate maximum thickness of the TL observed in microstructure surveys in multiple locations and seasons by *Sun et al.* [2013]. The INT region extends between the base of the TL and 200 m depth. These layers are illustrated for August 2008 ($j = 3$) in Figure 3.

In the TL and INT, where turbulence is assumed to be primarily locally driven [*Large et al.*, 1994], turbulent flux is parameterized as $\overline{w'(\theta, S)'} = -\kappa \partial(\theta, S)/\partial z$, where κ is a vertical eddy diffusivity. An unknown κ is estimated on the upper and lower interfaces of each TL bin [*LeVeque*, 2007, Figure 3]. In the INT, it is assumed that $\kappa = \kappa_{\text{INT}} = 10^{-5}$ m^2 s^{-1}, reflecting weak, internal wave-driven vertical diffusivity values typically observed
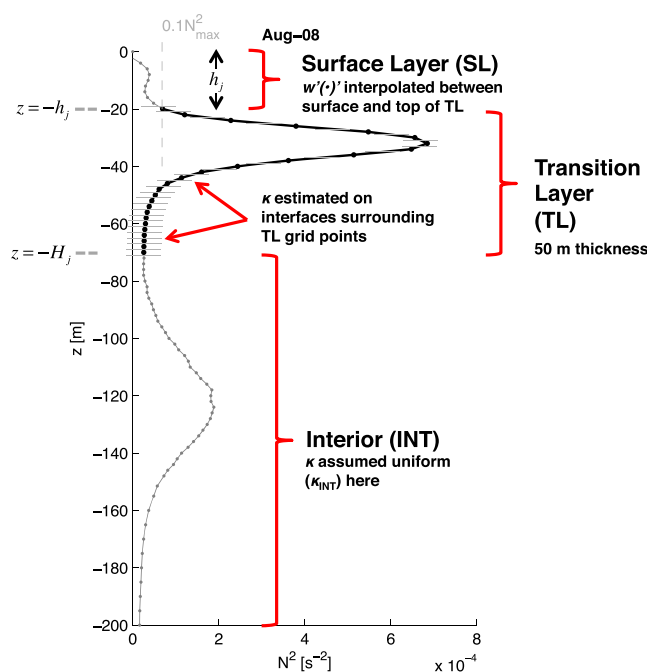
Figure 3. Monthly mean square buoyancy frequency N^2 in August 2008 (gray curve) and arrangement of least-squares problem vertical layers for this month (section 2.2). Markers in gray curve are N^2 values in each depth bin. The Transition Layer (TL) is bounded by depths $z = -h_j$ and $z = -H_j$ for time interval j, as shown at left. Diffusivities at the interfaces above and below transition layer depth grid points (indicated by solid black lines/points) are included in the vector of unknowns. The peak in N^2 centered at $z = -30$ m is the top of the seasonal thermocline, which is present in summer at Ocean Station Papa. The weaker peak at $z = -125$ m represents the salinity-stratified permanent halocline, which is present in all months (Figure 1).

in the upper deep ocean [*Ledwell et al.*, 1993; *Waterhouse et al.*, 2014]. This value is also consistent with lower boundary conditions used in one-dimensional models that have successfully simulated the upper-ocean annual cycle at OSP [*Large et al.*, 1994; *Large*, 1996].

In the SL, turbulence may be nonlocally driven, such as during surface buoyancy loss and free convection, which often invalidates the parameterization of turbulent flux as proportional to the vertical gradient and an eddy diffusivity there. No attempt is made to resolve the vertical structure of turbulent flux in the SL in this study. Instead, monthly turbulent flux profiles are assumed to vary linearly between the shallowest TL bin and the specified surface values from (3) and (4); equivalently, the net monthly convergence or divergence of heat and salt due to turbulent fluxes is assumed to be vertically constant in the SL. A linear flux profile was assumed because, as will be shown, vertical profiles of $\partial\theta/\partial t$ and $\partial S/\partial t$ within the SL, where the turbulent fluxes are most important, are nearly constant in most months,

suggestive of a vertically constant net convergence/divergence at monthly scales. For consistency, the solar radiation profile in the SL is also assumed to be linear in this scheme—although the instantaneous profile has an exponential vertical form [*Paulson and Simpson*, 1977], over monthly time scales, absorbed radiation is stirred and mixed vertically within the SL, such that the effective radiative absorption at monthly scales is more vertically uniform. It is therefore emphasized that the turbulent and radiative flux profiles obtained here are not intended to be representative of instantaneous conditions, but rather effective profiles averaged over a monthly scale.

It is also assumed that w varies linearly within the SL in each month ($\partial w/\partial z$ assumed constant) between a value of $w = 0$ at $z = 0$ and its value estimated by the solution and the top of the TL [*Large et al.*, 1986]. The results are not very sensitive to this assumption, since there is little vertical thermal or haline stratification within the SL, with the result that vertical advection there is a small term in the balances (1) and (2).

As a result of the above assumptions, the least-squares problem solves for turbulent diffusivity only within the TL, and for vertical velocity only within the TL and INT. This results in 1223 unknown w and 538 unknown κ values, which together with 3440 u, v values give a full set of 5201 unknowns.

2.2.3. Additional Constraints and Global System of Equations

To overconstrain the system, additional equations include information about the known or assumed properties of the solution elements. These will be referred to as the *dynamical equations*, in contrast to the *tracer equations* described in section 2.2.1. The reasoning in adding these equations was to make the minimum number of additional assumptions that would provide independent constraints on the slope and offset of the vertical profiles of u, v, and w estimated in each month, while also utilizing a priori estimates from PEC1. For the u and v elements, equations are included to penalize departures of the monthly vertical shear and top 200 m integrated transport in the solution from the initial estimates of these quantities in PEC1. Further equations penalize the divergence of w in the TL and INT for deviations from a steady, linear vorticity

balance appropriate for the weak flow observed at OSP during Seaglider surveys [*Rhines*, 1986; *Matear*, 1993, PEC1], $\beta v = f \partial w / \partial z$, where f is the Coriolis parameter, β its meridional gradient, and here v is estimated by the least-squares solution. These equations provide constraints on the shape of the w profile deeper than the SL; its offset is constrained by equations that penalize deviation of w from that expected in each month based on the assumption of a rigid lid and viscid, steady, linear vorticity balance in the Ekman layer forced by CCMP wind stress curl [*Cronin et al.*, 2013, 2015]:

$$w(z=-H_j^{Ek}) = -\frac{\beta}{f} \int_{-H_j^{Ek}}^{0} v \, dz + (\rho_0 f)^{-1} \nabla \times \vec{\tau}. \tag{7}$$

This balance assumes that advection of planetary vorticity due to meridional Ekman currents is negligible, and that the surface stress is not strongly modified by the surface geostrophic shear [*Cronin and Tozuka*, 2016]. In each month, the equation (7) is posed 25 m deeper than the base of the SL, at a depth denoted $z = -H_j^{Ek} \equiv -(h_j + 25m)$, at which the turbulent stress is assumed to vanish. This depth was chosen based on previous observations showing wind-forced Ekman currents, and implicitly, turbulent stresses, penetrating below the well-mixed SL [*Rudnick*, 2003].

Together, the dynamical constraints provide an additional 4723 equations. Appending these to the tracer equations results in a system of 8203 equations in 5201 unknowns, expressed in linear form as

$$\mathbf{A}\vec{x} = \vec{b} + \vec{\epsilon}, \tag{8}$$

where $\vec{x}$ is a 5201 × 1 vector of unknown u, v, w, and κ in all 20 monthly intervals, and $\mathbf{A}$ is a sparsely populated 8203 × 5201 matrix of coefficients of these unknowns. Each row of this matrix corresponds to one equation of the system, and the values in each column represent the coefficients of the unknowns that appear in that equation. As an example, in rows corresponding to the potential temperature equations discretized by (6), columns corresponding to u_{ij}, v_{ij} unknowns include $-\Delta t_j \partial \theta / \partial x |_{ij}$, $-\Delta t_j \partial \theta / \partial y |_{ij}$, respectively. Here $\vec{\epsilon}$ represents the 8203 × 1 vector of residual errors in each row of the system, and $\vec{b}$ is a vector of inhomogeneous terms. For tracer equations, these terms include θ or S changes from the time series onset and radiative fluxes as in (6), and may also include surface turbulent fluxes, or diffusive fluxes in the INT layer, depending on the depth level and month. In the dynamical equations, inhomogeneous terms include the expected values of vertical shear, transport, divergence, and vertical velocity.

2.3. Scaling and Inequality Constraints
The system is multiplied by a row-scaling matrix $\mathbf{W}^{1/2}$, giving

$$\mathbf{W}^{1/2}\mathbf{A}\vec{x} = \mathbf{W}^{1/2}\vec{b} + \mathbf{W}^{1/2}\vec{\epsilon}, \tag{9}$$

and the solution is taken to be the vector $\vec{x}$ that minimizes the norm of the scaled residuals, $\vec{\epsilon}^T \mathbf{W} \vec{\epsilon}$ where superscript T indicates a transpose, subject to the following inequality constraints:

$$\mathbf{H}\vec{x} \geq \vec{m}, \tag{10}$$

where $\mathbf{H}$ is a 538 × 5201 matrix and $\vec{m}$ is a 538 × 1 vector, both of which are specified such that all 538 TL diffusivities in the solution vector are required to be positive and at least as large as the assumed κ_{INT}. This constraint reflects known properties of stratified upper-ocean turbulence, in which diffusivity is positive and rapidly decays vertically from an elevated value at the base of the SL to weak interior values [e.g., *Sun et al.*, 2013].

The role of the matrix $\mathbf{W}^{1/2}$ is to normalize the system such that all residuals have similar dimensions. Ideally, it is chosen such that its matrix square $\mathbf{W}$ is the inverse of the covariance matrix of the residuals $\langle \vec{\epsilon}\vec{\epsilon}^T \rangle$ [*Wiggins*, 1972; *Wunsch*, 1978; *Olbers et al.*, 1985; *Zhang and Hogg*, 1992]. In practice, the residual covariance structure is not known a priori, and selection of $\mathbf{W}^{1/2}$ relies on some subjective judgment regarding the error structure [*Olbers et al.*, 1985; *Hogg*, 1987]. Here, in an approach similar to *Olbers et al.* [1985], $\mathbf{W}^{1/2}$ is specified as diagonal with each diagonal element chosen to be the product of two constants, one of which normalizes the residual based on the assumed error in the corresponding row of the system (8), while the

Table 1. Squared Row-Scaling Factors Applied to the System (9), by Equation Type[a]

Equation Type	Square Scaling Factor	Notes
$\theta(z,t)$	$\left(\frac{\Delta(z)}{200\text{m}}\right)\frac{1}{0.2\sigma^2(\theta(z,t))}$	$\sigma^2(\theta(z,t))$ indicates temporal variance of θ at depth z; $\Delta(z)$ is vertical thickness of bin centered at depth z.
$S(z,t)$	$\left(\frac{\Delta(z)}{200\text{m}}\right)\frac{1}{0.2\sigma^2(S(z,t))}$	
$\int_{-200\text{m}}^{0}\theta(z,t)dz$	$\frac{1}{0.2\sigma^2\left(\int\theta dz\right)}$	
$\int_{-200\text{m}}^{0}S(z,t)dz$	$\frac{1}{0.2\sigma^2\left(\int Sdz\right)}$	
$\partial u/\partial z,\ \partial v/\partial z$	$\left(\frac{\Delta(z)}{200\text{m}}\right)\frac{1}{\left[F_{0.95}^{-1}(z,t)\right]^2}$	$F_{0.95}^{-1}(z,t)$ is the estimated 95% upper bound on the magnitude of errors in vertical shear at depth z and at time t, based on errors in horizontal gradients of density (PEC1).
$\int_{-200\text{m}}^{0}udz,\ \int_{-200\text{m}}^{0}vdz$	$\frac{1}{(200\text{m}\times0.01\text{ms}^{-1})^2}$	Assumed depth-average current error of 0.01 m s^{-1}.
$\partial w/\partial z$	$\frac{\Delta(z)}{(200\text{m}-h_j)}\frac{1}{(1.7\times10^{-9}s^{-1})^2}$	Magnitude of omitted unsteady term in linear, inviscid vorticity balance, based on time-derivative of vertical vorticity of depth-average flow (PEC1). Scaling applied for bins centered deeper than $z=-H_j^{Ek}=-(h_j+25\text{m})$, the assumed depth at which turbulent stress ≈0 (section 2.2.3).
	$\frac{\Delta(z)}{(200\text{m}-h_j)}\left(\frac{\rho f H_j^{Ek}}{|\nabla\times\vec{\tau}|}\right)^2$	Magnitude of omitted viscous terms in $\beta v=f\partial w/\partial z$ balance scale as $\sim|W_{Ek}|/H_j^{Ek}$, where $|W_{Ek}|=|\nabla\times\vec{\tau}|/(\rho f)=0.088$ m d^{-1} is a characteristic Ekman velocity magnitude. Applied for bins shallower than $z=-H_j^{Ek}$.
$w(-H_j^{Ek})$	$\left(\frac{\rho f}{er(\langle\nabla\times\vec{\tau}\rangle)}\right)^2$	$er(\langle\nabla\times\vec{\tau}\rangle)=6.7\times10^{-7}$ N m^{-3} determined based on root-mean-square difference in monthly average wind stress between mooring and Cross-Calibrated Multi-Platform (CCMP) product; error in wind stress curl determined assuming error in each gradient component is independent, and has length scale given by CCMP grid resolution.

[a]The square root of these factors are the diagonal elements of the matrix $\mathbf{W}^{1/2}$. PEC1 refers to *Pelland et al.* [2016].

second accounts for the depth extent corresponding to each row. The scaling factors for each equation type are listed in Table 1.

For the dynamical equations, the assumed square errors are based on the estimated size of errors in geostrophic shear, horizontal transport, or wind stress curl, or in the case of equations governing $\partial w/\partial z$, the size of the omitted terms in the linear, steady vorticity balance (Table 1). For the tracer equations, the square error in each row is assumed proportional to the variance of θ or S at the corresponding depth level of that row. This choice was made because the time variance of each tracer differs between depth levels of the upper ocean (Figure 2). It is reasoned that for temperature, for example, a large error in a near-surface depth bin (where variance is large) and a small error in a depth bin near 200 m (where the variance is weak) should each contribute equally to the norm of the scaled residuals. Different proportions of the variance were tried as scaling factors; it was found that normalizing the tracer budget errors by 20% of the variance at each depth level gave scaled residuals in the tracer equations that were of similar dimension to those in the dynamical equations. This approach is similar to that used in the study of *Zhang and Hogg* [1992].

The scaled system (9) subject to the constraints (10) was solved using the "Problem LSI/LDP" algorithm described in *Lawson and Hanson* [1974, example given on p.170]. Diagnostics of the system (9), and description of the calculation of confidence bounds on the solution elements, are included in Appendix B.

3. Results

3.1. Tracer Residuals

Once a solution is obtained, using the governing equations, e.g., (6) for θ, the circulation and diffusivity in the solution $\vec{x}$ give an estimate of the change in potential temperature or salinity between the time series onset and any later time. It is convenient to add this value to the observed θ or S at the time series onset, to give a "solution estimate" of the monthly time record of each scalar variable—these are denoted $\hat{\theta}$ and $\hat{S}$,
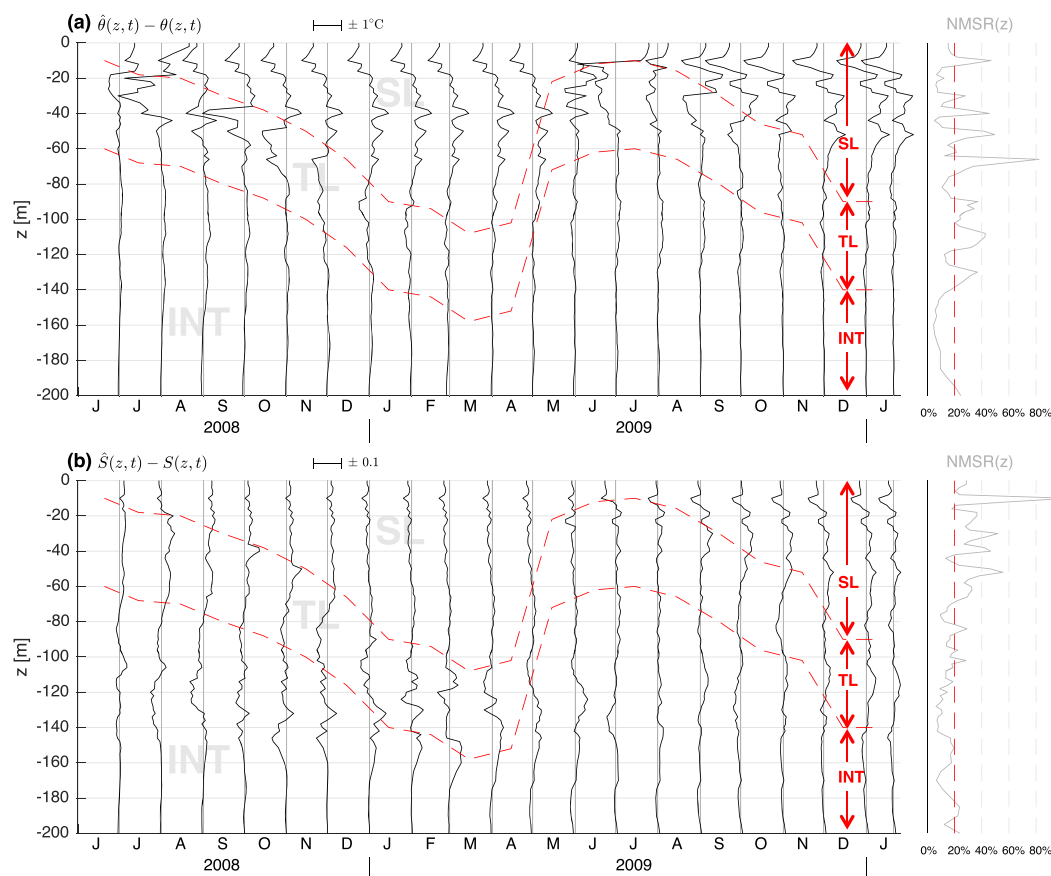
Figure 4. Residuals (a) $\hat{\theta} - \theta$ and (b) $\hat{S} - S$, where θ (S) is the observed potential temperature (salinity) and $\hat{\theta}$ ($\hat{S}$) are estimated by the least-squares solution. Black lines show profiles of the residuals at the end of each monthly time interval (scale at top left; 10 d = 1°C in Figure 4a and 0.1 parts per thousand in Figure 4b). Red-dashed lines indicate boundaries between vertical domains: SL = surface layer, TL = transition layer, INT = interior region (section 2.2). Gray profile plotted at right in each plot shows the normalized mean-square residual (NMSR), which is the mean-square error as a fraction of the time variance, as a function of depth. The red-dashed vertical line indicates an NMSR of 20%.

respectively. In effect, by seeking to minimize the square residual in the integrated tracer equations, the problem seeks to minimize the square difference $\hat{\theta} - \theta$ and $\hat{S} - S$.

Figure 4a shows profiles of residual for solution potential temperature ($\hat{\theta} - \theta$) at the end of all 20 time intervals. Solution residuals in general decrease vertically in accord with the time-variance of potential temperature, which follows from the formulation of the scaling factors as discussed in section 2.3. The majority (91.3%) of residuals are of magnitude of a degree or less, and the largest are found in the TL in Fall 2008 and throughout the TL and SL in the 1 July 2009 solution profile. The normalized mean-square residual (NMSR)—that is, the time-average square residual value in each depth bin, divided by the time variance of temperature in that bin—is 0.2 or less at 47 of 86 depth levels, and its vertical average is 0.194 if the varying thicknesses of each depth level are accounted for (0.210 without accounting for thickness; Figure 4a).

The structure of solution salinity residuals ($\hat{S} - S$) is more vertically uniform than that of potential temperature (Figure 4b). The greatest magnitude residuals are in the INT region, where salinity variance is also greatest, and in the TL region when the SL is deep enough that the TL extends vertically into the halocline (e.g., Winter 2009). Salinity NMSR is less than 0.2 at 46 of 86 depth grid points and thickness-weighted NMSR = 0.217. Salinity NMSR is generally elevated in the top 70 m in comparison to temperature (Figure 4b).

Figure 5 shows the solution potential temperature and salinity in comparison to the observations when averaged over four zones in the top 200 m. The first two zones (SL, TL) follow from the definitions described
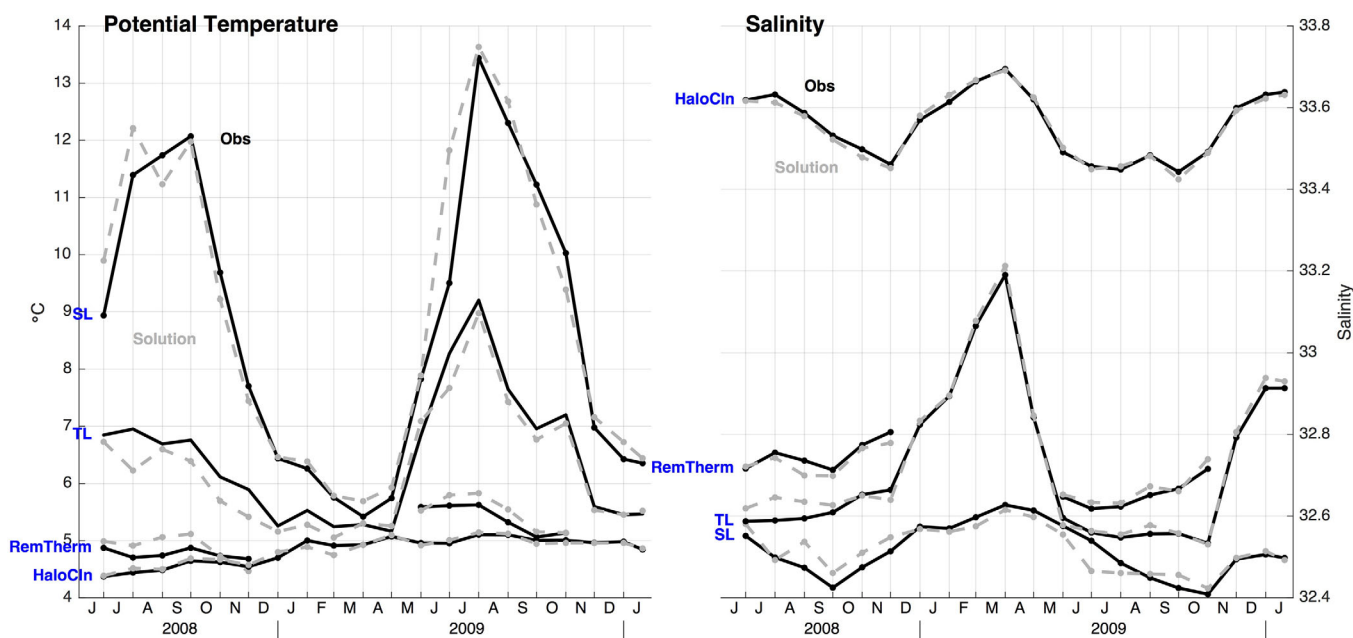
Figure 5. Temperature and salinity, averaged vertically in distinct zones. Black lines show observed values and dashed gray lines show those obtained from observed surface fluxes and transports from the solution to the system (9). Vertical averages are taken over four zones, in order of decreasing depth, the surface layer (SL), transition layer (TL), remnant thermocline (RemTherm), and halocline (HaloCln) as defined in the text.

above. The lower two zones are a partition of the INT region above and below 120 m—the upper of these two is referred to as the remnant thermocline (abbreviated RemTherm in this figure) and the lower of the two is denoted halocline (HaloCln). Note that there are times during the winter when the upper boundary of INT is deeper than 120 m and thus the remnant thermocline zone is undefined during these months (discontinuities in the remnant thermocline record displayed in Figure 5). When averaged over this vertical scale, the solution transports correctly reproduce the observed bulk vertical stratification in temperature and salinity for all time interval edge profiles except one: the solution remnant thermocline is cooler than the halocline by 0.11°C at 1 December 2008, while in the observations, the remnant thermocline is warmer by 0.14°C. Residuals for tracers integrated over the top 120 m or 120–200 m are discussed further in section 3.3.2.

3.2. Physical Transports
3.2.1. Three-Dimensional Circulation
Horizontal velocities estimated by the solution, $\vec{u}^{LS}$, are shown in Figure 6. These are compared to the geostrophic velocities reported in PEC1, $\vec{u}^g$, to which $\vec{u}^{LS}$ were constrained to be similar (section 2.2.3). In both $\vec{u}^g$ and $\vec{u}^{LS}$, the flow is nearly unidirectional in the top 200 m in each month, with progression of moderate poleward flow during the first 9 months of the time series that rotates counterclockwise and weakens over the remaining months (Figure 6). Solution velocities mostly fall within 1 cm s^{-1} of $\vec{u}^g$ (light gray ellipses), and have confidence bounds that are smaller than this value (Figure 6). Root-mean-square (RMS) magnitudes of the differences in velocity $|\Delta\vec{u}| = |\vec{u}^g - \vec{u}^{LS}|$ between the solution and estimates from PEC1 vary from 0.9 to 1.0 cm s^{-1} at each of the four depths considered in Figure 6. The RMS magnitude of the offset in 0–200 m depth average velocity between the solution and the estimates from PEC1 is 0.78 cm s^{-1}.

Profiles of vertical velocity estimated by the solution are shown in Figure 7. Profiles in the upper row (June 2008 to March 2009) exhibit a consistent increase with height, while those in the lower row (April 2009-on) appear nearly nondivergent, consistent with the time series of poleward flow and the steady, linear vorticity balance (section 2.2.3). In both time periods, the divergence within the interior is weak relative to the offset of each profile, and profiles of w are relatively uniform across the top 200 m with the exception of the SL. Dashed lines extending across the SL in Figure 7 reflect the interpolated vertical velocity within this zone (section 2.2.2). Vertical velocity profiles estimated by the least-squares solution have confidence intervals
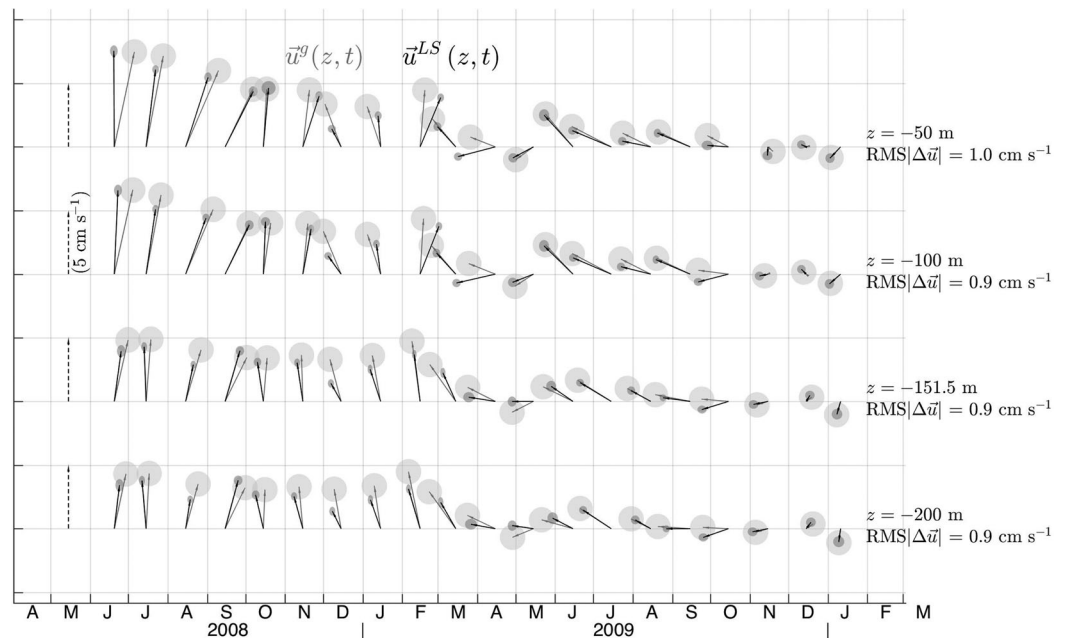
Figure 6. Horizontal velocities estimated by the least-squares solution ($\vec{u}^{LS}$, black) and geostrophic velocities reference to observed 0–1000 m depth-averaged current ($\vec{u}^g$, gray; reported in *Pelland et al.* [2016]) at four selected depths. Scale vector (dashed black; 1 cm s^{-1} = 10 d northward) at far left for each row. Text at right of each row indicates the depth of velocity estimates and the root-mean-square (RMS) magnitude of the difference between observed and solution velocities. Dark gray (light gray) ellipses represent confidence bounds for $\vec{u}^{LS}$ (1 cm s^{-1} for $\vec{u}^g$).

approximately ± 0.05 m d^{-1} with weak vertical structure; profiles are relatively more uncertain near the surface than at depth.

Upwelling 25 m below the SL (at $z = -H_j^{Ek}$, section 2.2.3) in the least-squares solution, denoted w^{LS}, varies by as much as 0.61 m d^{-1} month-to-month (Figure 8). Three additional time series are shown in this figure. The first of these, denoted w^{LS-}, is w^{LS} minus the effect of vortex stretching of the meridional velocity shallower than $z = -H_j^{Ek}$:

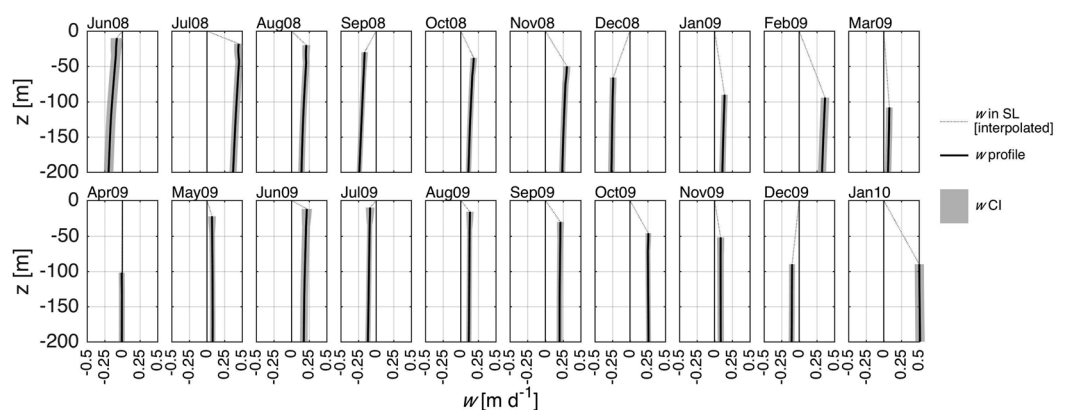$$w^{LS-} = w(z = -H_j^{Ek}) + \frac{\beta}{f} \int_{-H_j^{Ek}}^{0} v_j^{LS} dz, \tag{11}$$

Figure 7. Monthly profiles of vertical velocity w estimated by the least-squares solution (black curves), with confidence intervals (CI; gray shading). Dotted curves indicate the assumed w profile within the surface layer (SL) which is interpolated between the value estimated at the uppermost transition layer point and $w = 0$ at $z = 0$.
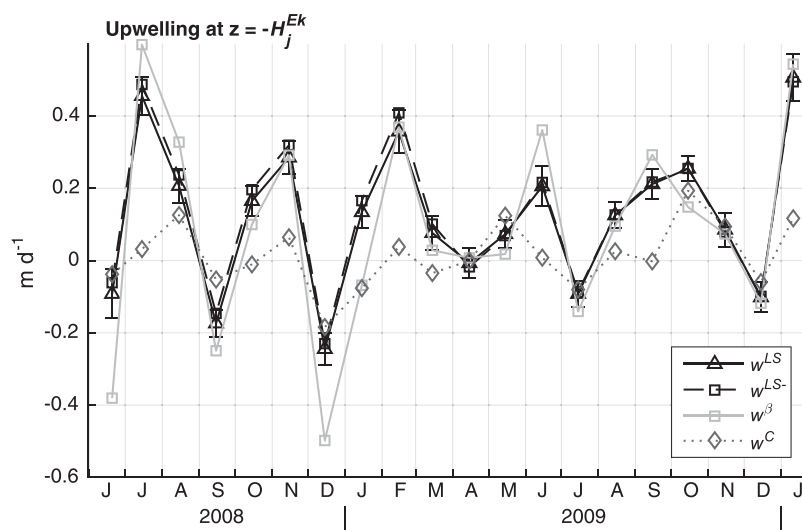
Figure 8. Vertical velocity w 25 m below the base of the SL, at $z = -H_j^{Ek}$. Vertical velocity estimated from the least-squares solution is denoted w^{LS} (black curve with triangle markers); whiskers indicate its confidence interval in each month. This is compared to three additional time series, described in section 3.2.1: w^{LS} minus the effect of vortex stretching shallower than $z = -H_j^{Ek}$ (w^{LS-}), upwelling estimated independent of the least-squares solution (w^β), and upwelling expected due to wind stress curl (w^C).

which by (7) is the quantity that is most comparable to the estimated wind stress curl. Here v_j^{LS} is the meridional velocity estimated by the least-squares solution in monthly interval j. In this case, accounting for the upwelling due to meridional flow shallower than $z = -H_j^{Ek}$ results in a negligible correction to w^{LS}. The second additional time series, denoted w^β, is an estimate of w at $z = -H_j^{Ek}$ formed under the estimate of purely linear flow ($\beta v^g = f \partial w^\beta / \partial z$, with v^g estimated in PEC1), referenced such that density is nearly conserved in the stratified halocline; i.e., vertical advection of density must as close as possible balance the horizontal advection due to $\vec{u}^g$ and time rate-of-change. The variations in w^β clearly correlate with those in w^{LS}, though have differences in each month of up to 0.29 m d^{-1}. The final curve in Figure 8 is the expected upwelling due to monthly average wind stress curl calculated from the CCMP product, $w^C = (\rho f)^{-1}(\nabla \times \vec{\tau})$. The month-to-month variations in corrected w^{LS-} correlate with w^C (correlation coefficient $r = 0.63$; $t = 3.45 > t_{0.975} = 2.09$ for $v = 19$ using a two-sided Student's t test), but with gain of 1.45:1 and a net positive offset. Mean estimated upwelling at $z = -H_j^{Ek}$ during the time series is 0.116 m d^{-1} (42.5 m yr^{-1}) while the mean estimated upwelling due to CCMP wind stress curl is 0.013 m d^{-1} (4.7 m yr^{-1}).

3.2.2. Diffusivity and TL Structure

The estimated diffusivity profiles in the TL exhibit consistent shape and amplitude throughout the Seaglider survey time series (Figure 9). Diffusivity κ approaches 10^{-3} m^2 s^{-1} at the top of the TL and quenches rapidly with depth in the seasonal thermocline or halocline. The depth of maximum stratification in the TL (stratification profiles are indicated by background shaded curves in Figure 9) forms a consistent boundary above which the steepest decreases with depth in κ are estimated by the least-squares solution. The slope of $\log_{10}(\kappa)$ indicates a decay with depth in this range of about a decade per 10 m.

Confidence intervals on κ indicate that this variable is also best resolved by the least-squares solution shallower than the depth of peak stratification (Figure 9b). At the top of the TL, confidence bounds on κ are small in most months and exclude the assumed κ_{INT} in all months except September 2008 and April 2009. These confidence bounds are small to a greater depth in the TL during October 2008 to March 2009, and November 2009, which is in conjunction with a greater depth of maximum stratification in those months (Figure 9b).

The consistent vertical structure of the decay of diffusivity with depth from the peak value at the top of the TL is evident in a composite of monthly diffusivity profiles (Figure 10a). In this figure, each profile has been normalized (κ_{norm}) by subtracting the assumed κ_{INT} and dividing by the profile amplitude, that is, the amount by which the peak diffusivity at the top of the TL (κ_h) is elevated above the interior diffusivity:
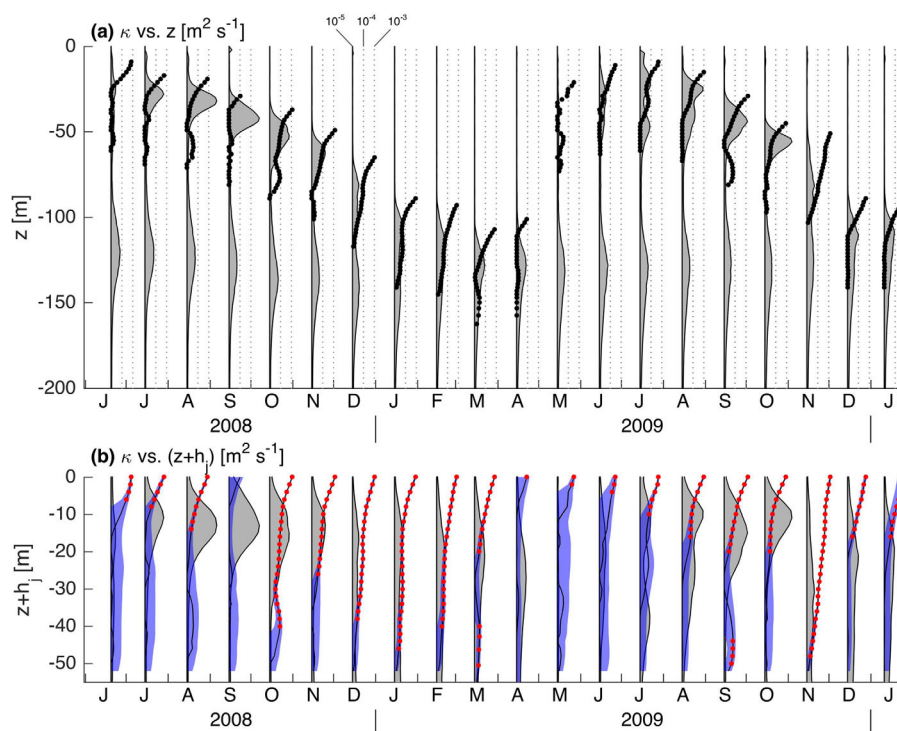
Figure 9. Vertical eddy diffusivity κ estimated by the least-squares solution, versus (a) height and (b) height above the transition layer (TL) top. In Figure 9a, black dots indicate profiles of κ (estimated only in TL), plotted on a logarithmic scale relative to the center of each time interval. Solid line in each month indicates the assumed deep κ_{INT} value of 10^{-5} m² s⁻¹. Gray-dotted grid lines indicate diffusivity increases of 1 and 2 decades, respectively (labeled at top for December 2008). Background-shaded profiles indicate the monthly average square buoyancy frequency profile (first dotted line = 2.5×10^{-4} s⁻²). In Figure 9b, blue-shaded regions indicate confidence bounds on κ. Red dots indicate portions of the κ profile where the confidence bounds exclude κ_{INT}.

$$\kappa_{norm} = \frac{\kappa - \kappa_{INT}}{\kappa_h - \kappa_{INT}}. \tag{12}$$

This normalization is chosen to isolate the structure of the decay with depth of diffusivity in each profile, independent of the profile maximum value. The vertical coordinate is the height above the TL top ($z_{TL} \equiv z + h_j$), which aligns all 20 months. Normalized profiles exhibit an approximately exponential decrease from the peak values at the base of the SL. Fitting an exponential to the profile for each month gives e-folding scales that vary from 2.4 to 10.3 m, with a mean value of 4.5 m. If a mean profile is first constructed, and an exponential fit to this profile, the e-folding scale is 4.4 m. Deeper than ∼20 m below the SL, the profiles do not decay quite as quickly as an exponential function (Figure 10a), though as noted above, the profiles are not well-resolved there in most months. Shallower than 15 m the exponential is a very good approximation. A power-law curve with form $\hat{\kappa} = c_1 \times [-(z+h)]^{-c_2}$ gave better results when fitted to the mean profile for $z_{TL} \leq -10$ m. The best-fit power-law curve had coefficients $c_1 = 2.05$ and $c_2 = 1.27$.

The stratification and κ_{norm} profiles in Figures 10b and 10c are divided into two corresponding seasonal groupings, based on visual inspection and seasonal changes in TL stratification. High stratification profiles (red lines in Figures 10b and 10c) correspond to July–November 2008 and July–October 2009 (labeled "summer/fall"). The summer/fall diffusivity profiles estimated by the solution decay more rapidly with depth than the profiles from other months (Figure 10c). The composite summer/fall profile has an e-folding scale of 3.3 versus 5.3 m for the winter/spring profiles.

Figure 11 shows the diffusivity estimated at two depths within the TL: at the level of peak N^2 within the TL, and at the top of the TL/base of the SL, the shallowest depth bin greater than 10 m at which N^2 is 10% of its peak value (section 2.2.2). The weakest diffusivities are estimated during the spring restratification period (April and May of 2009) and during September 2008, while the highest diffusivities are estimated in October–December 2008, and August–November 2009. The mean κ at the top of the TL in October–December during Seaglider surveys was estimated to be a factor of 1.69 larger than during June–August.
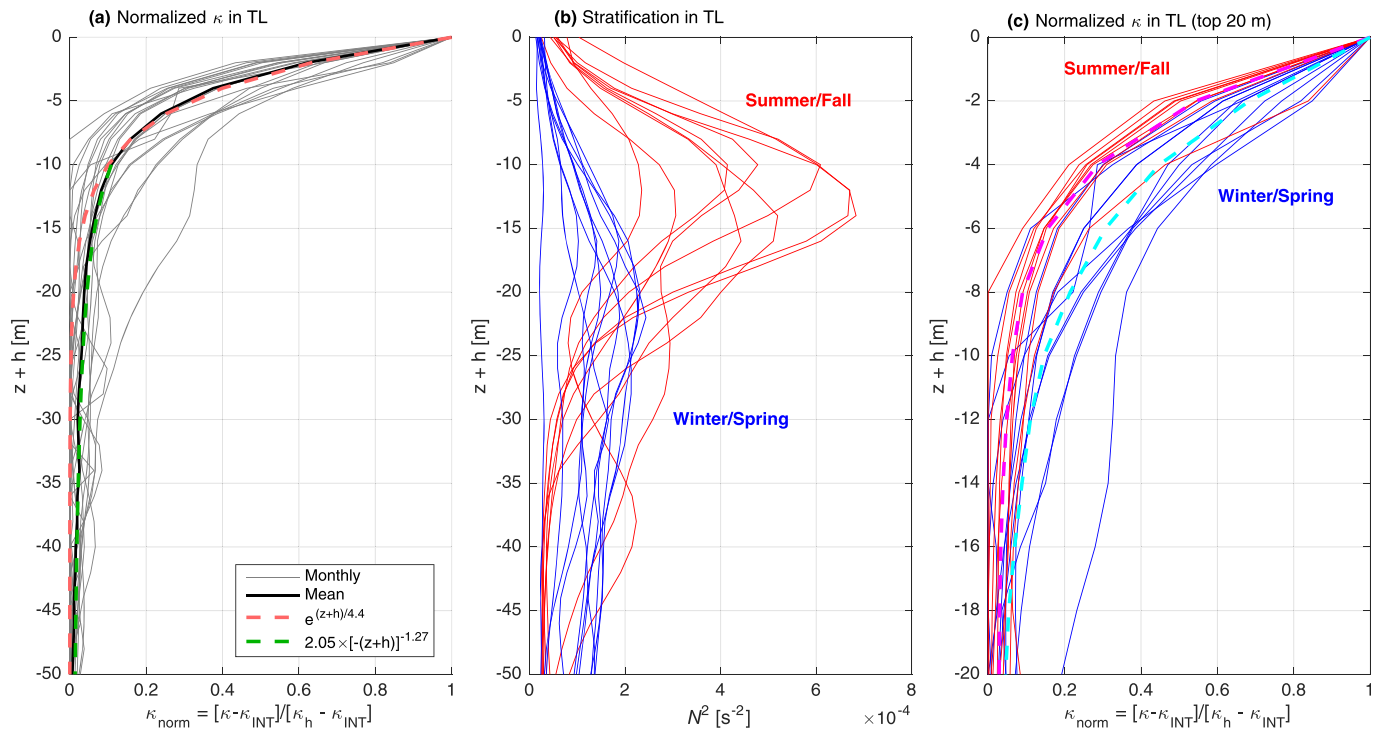
Figure 10. Profiles of (a and c) normalized κ and (b) square buoyancy frequency (N^2) in the transition layer (TL). Profiles plotted versus height above the TL upper boundary. Profiles in Figures 10a and 10c are normalized by subtracting the assumed deep diffusivity κ_{INT}, and dividing by the residual amplitude (peak value of the profile after κ_{INT} is removed). In Figure 10a, the solid black curve is a mean profile and the dashed red curve is an exponential fit to the mean profile. The green-dashed curve is a power-law fit to the mean profile below 10 m. In Figures 10b and 10c, red profiles indicate high-stratification profiles (July–November 2008, July–October 2009). Blue profiles indicate low-stratification profiles from other months. Note that Figure 10c displays the upper 20 m of the transition layer only. In Figure 10c, the thick cyan-dashed line (thick magenta dashed line) is the mean κ profile for the low-stratification (high-stratification) months in the top 20 m.

3.3. Heat and Salt Balances

3.3.1. Depth-Resolved Balances

The estimated advection, diffusion, and storage terms in the θ and S balances (1) and (2) are shown in Figures 12 and 13. The advection and diffusion terms are obtained from the solution elements, while the local
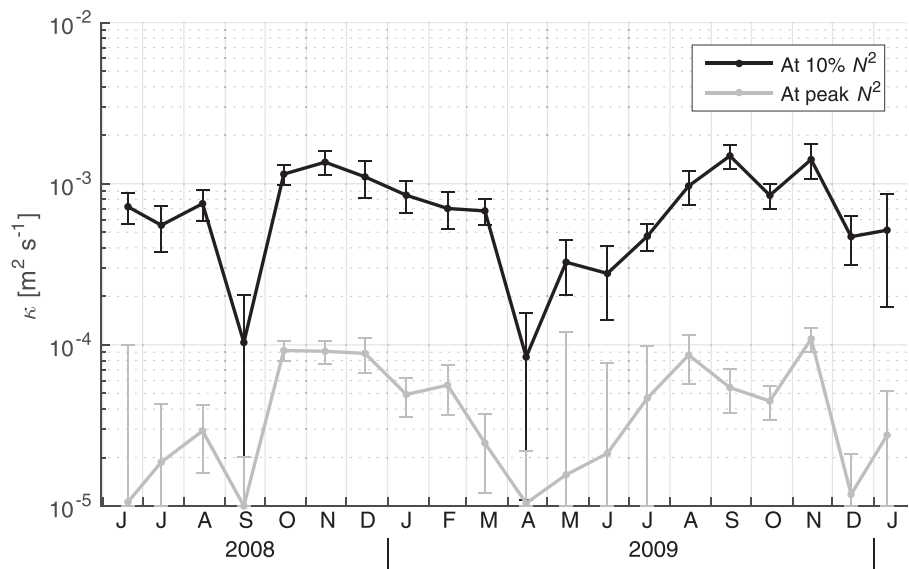

Figure 11. Diffusivity estimated from the least-squares solution at two locations within the transition layer (TL). The black line shows diffusivities at the top of the TL (defined as the first depth bin greater than 10 m at which the square buoyancy frequency N^2 is at least 10% of its peak value). The light gray line shows diffusivities at the depth of peak N^2. Whiskers indicate confidence bounds.
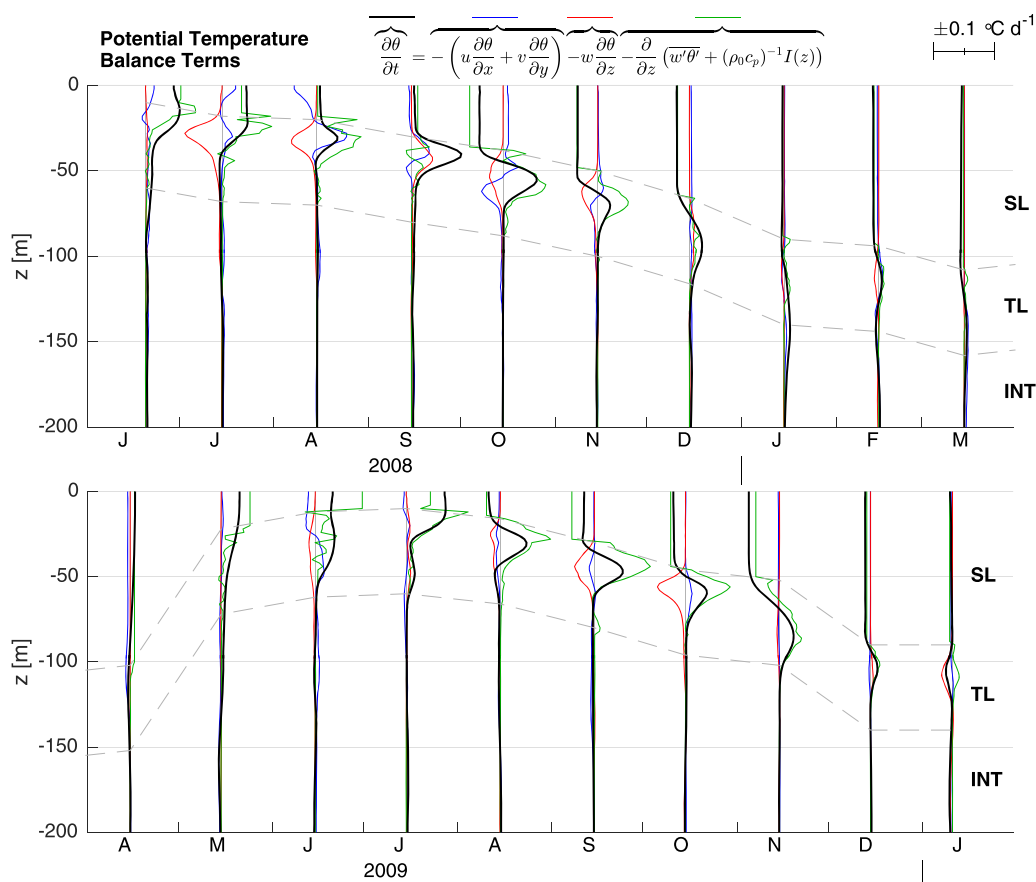
Figure 12. Estimated terms in the monthly upper-ocean potential temperature θ balance (equation at top), (top) June 2008 to March 2009 and (bottom) April 2009 to January 2010. In each month, vertical profiles of the resolved terms are plotted in an x coordinate system with origin at the center of each month. Blue curves indicate horizontal advection, red curves vertical advection, green curves the convergence of turbulent flux plus absorption of solar radiation, and black curves are the local tendency. Curves are plotted with the sign convention of the equation above the top plot; i.e., positive red curve indicates an import of warm water/removal of cool water due to horizontal advection. Gray-dashed lines indicate boundaries between vertical domains: SL = surface layer, TL = transition layer, and INT = interior region (section 2.2).

storage is estimated as the difference between vertical profiles at the beginning and end of each monthly interval (described in section 2.1). The profiles of estimated turbulent flux given by the least-squares solution, along with specified solar radiation, are shown in Figure 14.

In the θ balance, the estimated local storage terms (black curves) are largest in the SL and TL (Figure 12), reflecting the annual cycle of summer warming of a thin, stratified SL followed by cooling and deepening of the TL in the fall and winter (Figure 2). In most months, the local storage term in the SL and TL is primarily balanced by the combined convergence or divergence of turbulent flux and absorption of solar radiation (both terms included in the green curve in Figure 12). In all months, the absorption of solar radiation adds heat to the SL, as evident from the convergent downward radiative flux profiles (green curves in Figure 14a). In contrast, the turbulent flux of heat (red curves in Figure 14a) acts to remove heat from the SL in all months. This is due to the downward export of heat from the SL to upper TL due to turbulent diffusion, and the loss of heat at the surface to the atmosphere due to longwave, latent, and sensible components of surface flux, which give the upper boundary condition for the turbulent flux of heat in each month (section 2.2.1). In summer, a net heating of the SL occurs because the turbulent loss of heat from the SL to the atmosphere and TL is overwhelmed by the radiative absorption, while the opposite is true in autumn and winter as the SL cools (Figure 14a). Figure 14a indicates that, under the assumption of type IA water, a significant penetration of solar radiative flux to the TL occurs in the months May–August, which augments the heating of the upper TL due to downward turbulent diffusion from the SL. The latter process exports heat from the SL to progressively greater depths during each year as this layer increases in thickness, and is responsible
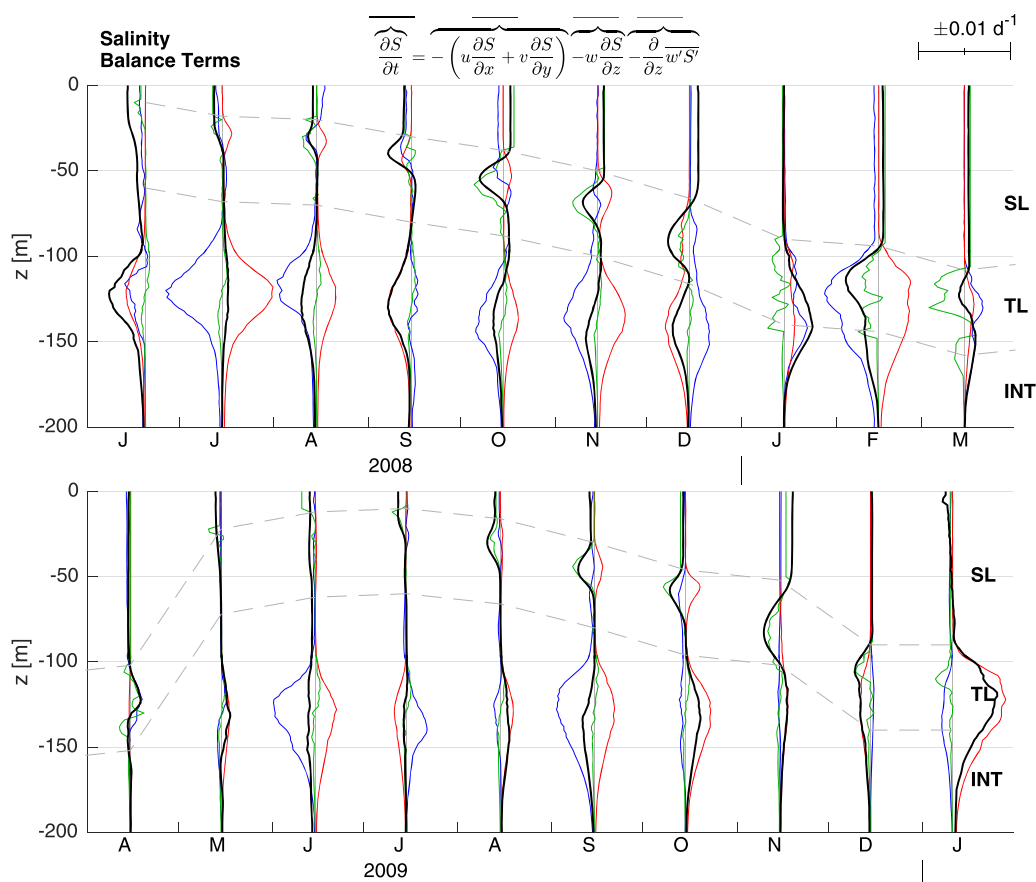
Figure 13. Estimated terms in the monthly upper-ocean salinity S balance (equation at top), (top) June 2008 to March 2009 and (bottom) April 2009 to January 2010. Terms are plotted as for potential temperature in Figure 12, with the exception that the green curve represents only the convergence of the turbulent flux of salt.

for the maximum in the annual temperature cycle occurring at later times as depth increases (Figure 2; PEC1).

In some months, vertical advection of heat (red curves in Figure 12) in the TL is of comparable magnitude to the net convergence or divergence of turbulent flux and solar radiation there (e.g., July–November 2008 and September–October 2009). The presence of the maximum magnitude of the vertical advection term in the TL reflects the estimated weakly divergent, hence nearly vertically constant, profiles of w deeper than the SL and the large vertical gradients of θ in the TL, especially in summer (Figure 2; PEC1). As will be discussed further in section 3.3.2, the net effect of this advection over the time series is an upwelling of cool water; this upwelling is evident, in particular, in monthly θ balances for July–August, October–November 2008, and September–October 2009 (Figure 12). Vertical advection of θ is negligible in the SL due to weak vertical gradients there.

Like vertical advection, horizontal advection of heat (blue curves in Figure 12) is also estimated to be an important term in the TL and SL in some months. This is evident in the SL in June–August 2008 and June 2009, and in the TL in July–October 2008 and June 2009. A net cooling in the SL or TL due to horizontal advection is evident in the lower TL in October–November 2008 (Figure 12). However, as will be shown in section 3.3.2, the net effect of this advection is small in the upper 120 m time-integrated balance. The balance of terms for θ deeper than 120 m depth, which is not visible in Figure 12 due to the small magnitude of all terms relative to those in the upper 120 m, will be discussed in the following section.

In contrast to θ, the terms that compose the estimated salinity balances during Seaglider surveys were greatest in magnitude deeper than 100 m, where salinity dominates the density stratification (Figure 13). In
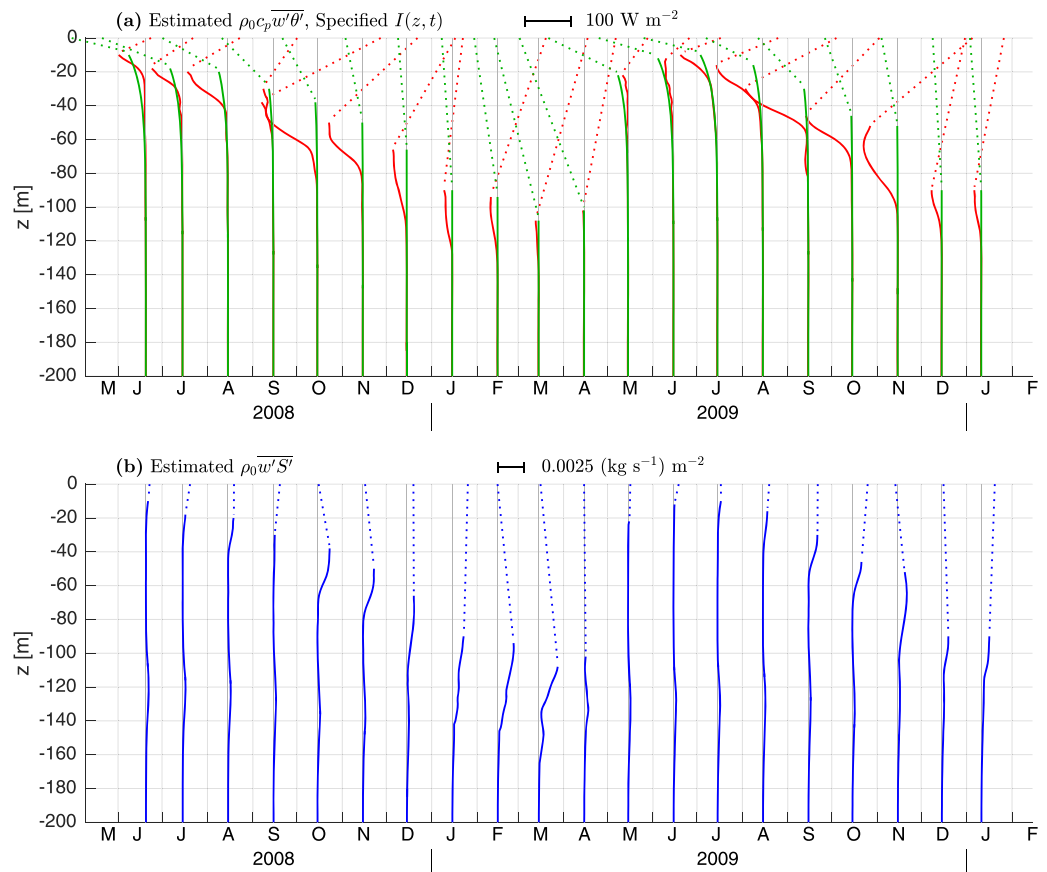
Figure 14. Monthly profiles of (a) vertical turbulent and radiative heat fluxes and (b) turbulent salt fluxes. In Figure 14a, red curves are the turbulent fluxes estimated by the least-squares solution, while green curves are the radiative flux profiles specified from observations. As in Figure 1, profiles are, respectively, scaled in proportion to the thermal expansion/haline contraction coefficients appropriate for average conditions at the surface, such that two curves of equal size in Figures 14a and 14b are approximately equal in their contribution to vertical buoyancy flux. Dashed portions are within the surface layer, where fluxes are interpolated between the surface value and the top of the transition layer (section 2.2.2).

this depth region, the observed local storage (black curve in Figure 13) during the Seaglider time series was dominated by secular rather than annual-period variability, as evident in Figure 2. Both horizontal (blue curves) and vertical (red curves) advection are estimated to be important to the salinity balance in the halocline, while the estimated convergence of turbulent salt flux (green curves) is comparably much smaller with the exception of the months January–April 2009, when the TL and associated large turbulent fluxes extended into the upper halocline. The net local storage/removal of salt in the halocline is often estimated to be the small difference between much larger horizontal and vertical advection (e.g., July 2008, June 2009). While the convergence of turbulent flux is generally secondary in the INT region, where it is assumed $\kappa_{INT} = 10^{-5}$ m s^{-1}, close inspection of the green curves in Figure 13 reveals that this term consistently acts to locally increase the salinity in the halocline above $\sim$125 m depth and decrease the salinity below this depth.

Estimated S balance terms are small in the SL though are larger in the TL and increase in magnitude there as the summer and fall progress, reflecting an increase in haline stratification in the TL (Figures 13 and 14b). As with θ, the observed local storage of S in the SL and TL is often primarily balanced by the net convergence of the turbulent salt flux, with occasional important local contributions from horizontal or vertical advection, especially in the TL (e.g., October 2009 in Figure 13). The estimated turbulent flux of salt does not consistently act to remove or add salt to the SL in all months, in contrast to the consistent net removal of heat there (Figure 14b). The salinity stratification is such that there is an upward turbulent flux of salt at the base of the SL in all months, and an upward "virtual" flux of salt at the ocean surface by the boundary condition (4) in most months, due to a relatively steady net surface moisture flux from atmosphere to the

ocean, as will be shown below. The surface flux tends to be larger than that at the base of the SL in summer and fall, when the SL is thin and salinity stratification at its base is weak, leading to a net freshening of the SL due to turbulent flux (Figure 14b). The opposite is generally true in the fall and winter as the SL deepens and the salinity stratification increases at its base, resulting in large upward turbulent fluxes of salt there (alternately, downward fluxes of freshwater). The relative size of the curves in Figures 14b and 14a, which are scaled such that a curves of equal size between the two plots in Figure 14 contribute equally to the turbulent flux of buoyancy, indicates that turbulent flux of heat dominates the buoyancy flux in the SL and TL with the exception of winter 2009.

3.3.2. Vertically Integrated Balances

The 120 m depth surface marks an approximate boundary between the permanent halocline and the temperature-stratified upper ocean (Figure 1). Figure 15a shows the top 120 m heat balance, integrated in time from the start of the Seaglider surveys (t_0). This balance takes the form
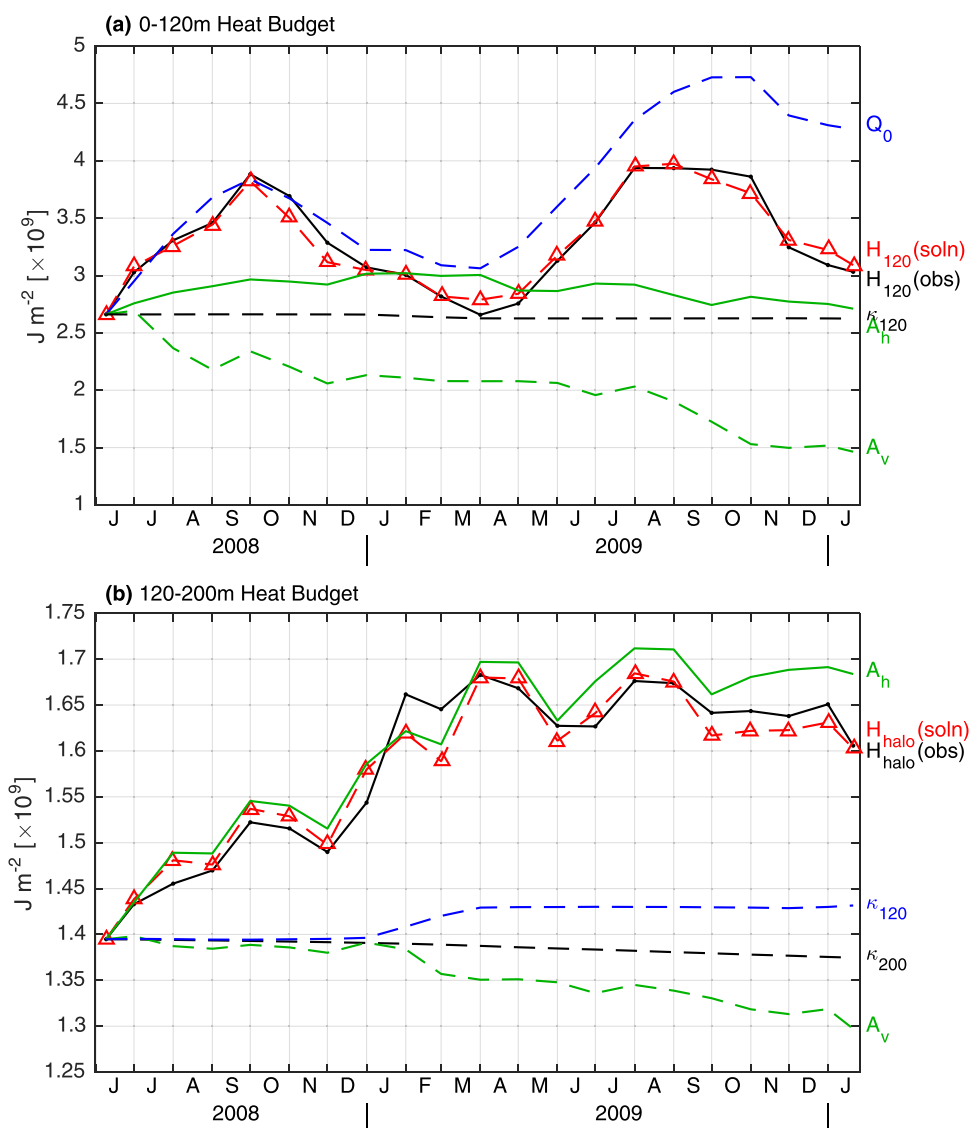

Figure 15. Time-integrated balances of heat during the array time series for (a) the top 120 m and (b) halocline region. Black lines indicate the record of observed heat content in each region [H(obs)]. Red-dashed lines indicate solution heat content [H(soln)]. Terms composing H(soln) are also shown: blue lines indicate heat flux crossing the upper boundary of each zone (surface heat flux Q_0 in Figure 15a, diffusion at 120 m κ_{120} in Figure 15b). Black-dashed lines show lower boundary heat flux (κ_{120} in Figure 15a, κ_{200} in Figure 15b). Solid green lines indicate horizontal advection (A_h), dashed green lines indicate vertical advection (A_v). These terms are defined for the top 120 m balance by (13).
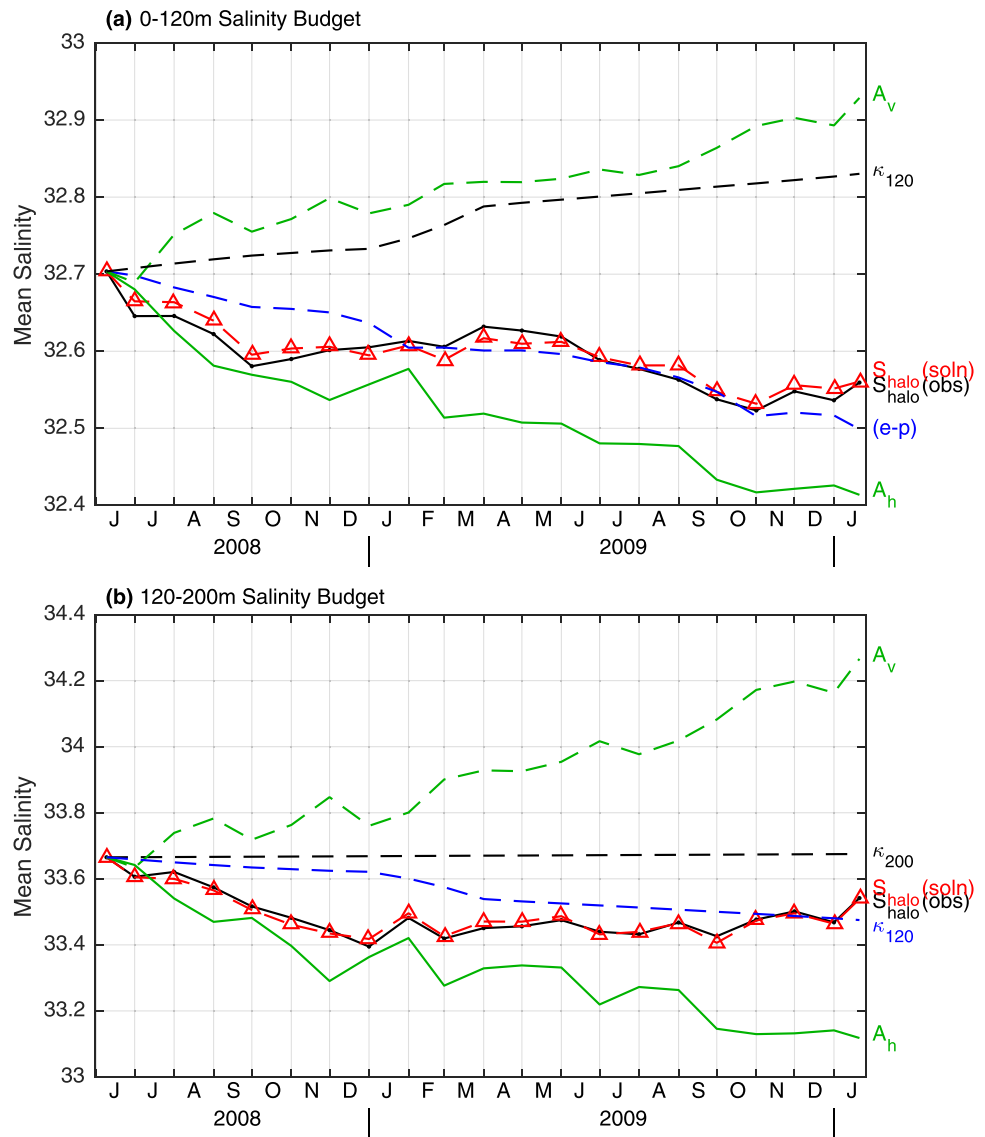
Figure 16. Time-integrated balances of salinity during the array time series for (a) the top 120 m and (b) halocline region. In each plot, black lines indicate the record of observed mean salinity in each region [S(obs)]. Red-dashed lines indicate solution mean salinity [S(soln)]. Terms composing S(soln) are also shown: blue lines indicate change in mean salinity due to salt flux crossing the upper boundary of each zone (surface moisture flux (e-p) in Figure 16a, diffusion at 120 m κ_{120} in Figure 16b). Black-dashed lines show change in mean salinity due to lower boundary salt flux (κ_{120} in Figure 16a, κ_{200} in Figure 16b). Solid green lines indicate horizontal advection (A_h) and dashed green lines indicate vertical advection (A_v).

$$
\rho_0 c_P \underbrace{\int_{-120\text{m}}^{0} \theta(z,t)\,\mathrm{d}z}_{H_{120}(t)} = \rho_0 c_P \underbrace{\int_{t_0}^{t}\int_{-120\text{m}}^{0} \left[-u(z,\tau)\frac{\partial\theta}{\partial x}(z,\tau) - v(z,\tau)\frac{\partial\theta}{\partial y}(z,\tau) \right] \mathrm{d}z\,\mathrm{d}\tau}_{A_h}
$$

$$
+ \rho_0 c_P \underbrace{\int_{t_0}^{t}\int_{-120\text{m}}^{0} \left[-w\frac{\partial\theta}{\partial z}(z,\tau) \right]\mathrm{d}z\,\mathrm{d}\tau}_{A_v} + \underbrace{\int_{t_0}^{t} \left[-\rho_0 c_P \overline{w'\theta'}_0(\tau) - Q_S(\tau) \right]\mathrm{d}\tau}_{Q_0} \tag{13}
$$

$$
+ \rho_0 c_P \underbrace{\int_{t_0}^{t} \left[-\kappa(-120\,\text{m},\tau)\frac{\partial\theta}{\partial z}(-120\,\text{m},\tau) \right]\mathrm{d}\tau}_{\kappa_{120}} + \rho_0 c_P \int_{-120\text{m}}^{0} \theta(z,t_0)\,\mathrm{d}z,
$$

where underbraces indicate the labels applied to each term in Figure 15a, and recall that Q_S is the short-wave component of net surface heat flux into the ocean, whose time integral is denoted Q_0. The balance (13) omits the negligible absorption of solar radiation below 120 m. The observed top 120 m heat content [$H_{120}(t)$, left-hand side of (13)] at the beginning and end of each monthly time interval is indicated by the black line in Figure 15a. On the right-hand side of (13), the least-squares solution allows estimation of the horizontal and vertical advective terms (A_h, A_v) and turbulent diffusion at 120 m (κ_{120}), while Q_0 is specified. The sum of these terms, plus the heat content at the time series onset (final term on the right-hand side of (13)), is the least-squares solution estimate of the top 120 m heat content time evolution. This is shown in red in Figure 15a; other curves show the individual components A_h, A_v, κ_{120}, and Q_0.

The solution results show that the top 120 m heat balance is between surface fluxes, local storage, and vertical advection during the Seaglider surveys at OSP (Figure 15a). The estimated net surface heat flux during Seaglider surveys was 32.4 W m^{-2} from the atmosphere to the ocean, while the upper 120 m warmed at an average rate of 7.3 W m^{-2}. The least-squares solution estimate indicates that the offset between surface fluxes and the observed storage of heat in the top 120 m is mainly closed by upwelling of cool water (Figure 15a). The net upwelling of cool water during the time series appears to result from the coincidence of strong upwelling with strong vertical gradients in temperature in summer and fall: the strongest cooling due to A_v occurs in July–August 2008, and August–October 2009 (Figure 15a). In nearly all other months, vertical advection has much less impact. Horizontal advection adds heat during the first half of the time series (13.5 W m^{-2}, 10.4 W m^{-2} of which is in the TL/SL), then removes heat (–10.6 W m^{-2}, -9.5 W m^{-2} of which is in the TL/SL), such that the net effect over the duration of the time series is weakly positive.

Figure 15b shows the results for a vertically integrated heat balance between 120 and 200 m depth. Estimated horizontal advection of heat from the east (PEC1) accounts for nearly all of the observed temperature changes in the halocline (Figure 15b). Upwelling removes some heat but is much less effective at cooling this portion of the water column per unit vertical velocity because of weak vertical temperature gradients in the salinity-stratified halocline (Figure 1, PEC1). Downward flux of heat into this zone from diffusion at 120 m is a secondary term. Turbulent diffusion at 200 m is very small, though this is a byproduct of the assumed $\kappa_{INT} = 10^{-5}$ m^2 s^{-1} there.

In the top 120 m salt balance, both horizontal and vertical advection are important—the least-squares solution estimates indicate horizontal advection of fresh water from the south and east (PEC1) nearly cancels upwelling of saline water and the upward diffusion of salt across the 120 m boundary, meaning the observed changes in top 120 m salinity are approximately those given by the net moisture flux from the atmosphere into the ocean, estimated to be 0.127 cm d^{-1} during Seaglider surveys (Figure 16a). Deeper than 120 m, vertical advection acts to increase the mean salinity, while horizontal advection and diffusive transport at 120 m add freshwater during the time series (Figure 16b). Diffusion of salt at 200 m is estimated to be a negligible term under the assumed κ_{INT}.

4. Discussion

4.1. Character of Balances

The estimated monthly balances of heat and salt during Seaglider surveys at OSP are consistent with previous observational studies in the southern GOA in that, within the SL and TL, turbulent flux, radiative absorption, and vertical advection terms generally dominate over horizontal advection in determining the local storage of heat and salt [*Denman and Miyake*, 1973; *Davis et al.*, 1981a; *Large et al.*, 1986; *Paduan and deSzoeke*, 1986; *Paduan and Niiler*, 1993; *Torruella*, 1995; *Ren and Riser*, 2009; *Cronin et al.*, 2015]. However, when considering balances integrated vertically and through time, contrasts are apparent between this study and the conceptual annual cycle discussed in section 1. First of all, the top 200 m was not in a steady state, with a net heating and freshening observed in both the 0–120 m and 120–200 m depth ranges. The roles of horizontal and vertical advection also differed from what was expected based on previous studies. Upwelling rather than horizontal advection removed the excess heat input from the atmosphere to the top 120 m. Horizontal advection was responsible for all of the net warming in the halocline, a small net heating in the top 120 m, and imported relatively fresh water throughout the upper 200 m. This import of fresh water helped to balance the input of saline water due to upwelling and diffusion.
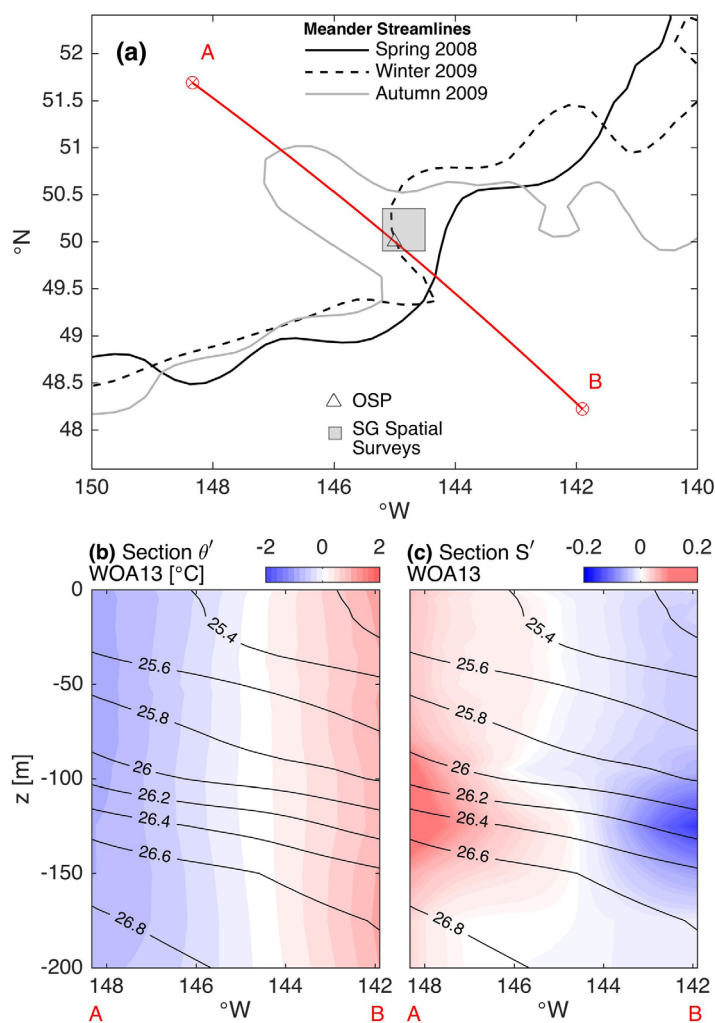
Figure 17. (a) Time-varying orientation of the meander of the mean flow during Seaglider (SG) surveys at Ocean Station Papa (OSP), illustrated by selected contours of seasonal-average sea surface height [*Pelland et al.*, 2016]. Section A-B is chosen to be orthogonal to the direction of the mean flow and along the axis of meander growth. Surveys took place within the shaded gray area. (b) Potential temperature θ' and (c) salinity S' anomalies in the upper 200 m along section A-B in the World Ocean Atlas 2013 (WOA13) climatology, with contours of potential density. Anomalies are computed on depth surfaces relative to a section-mean vertical profile.

These departures from the conventional balance took place during a meander of the North Pacific Current that allowed water from the subtropical-subarctic transitional domain equatorward of OSP to reach the Seaglider survey region (PEC1). Figure 17 shows the orientation of the meander at the beginning, middle, and end of the surveys (Figure 17a), along with potential temperature and salinity anomalies along a section taken orthogonal to the mean flow and along the main axis of the meander through the WOA 2013 climatology (Figures 17b and 17c). The anomalies are computed on surfaces of constant depth, relative to a section-mean vertical profile. It is clear that climatologically, water in the transitional domain is uniformly warmer, fresher, and therefore less dense along depth surfaces in the top 200 m. A horizontal displacement of transitional domain water toward OSP would be consistent with a horizontal import of warm and fresh water, as was estimated here, and a downward vertical displacement of isopycnals, as was noted in PEC1. This supports the idea that the meander of the mean flow was the principal source of the anomalous horizontal fluxes of heat and salt estimated in this study.

The role of vertical advection of heat and salt in depth-integrated balances was also in contrast to expectations, though its connection to the meander is less clear (see discussion in the following section). Fluctuations of w during Seaglider surveys were important for generating monthly variations in vertical heat and salt advection that were of opposite sign to the survey-average values; these had a significant impact on the character of the total balances of potential temperature (salinity) in the seasonal thermocline (halocline), where vertical gradients are large. It is likely that such variations would similarly impact the balances of other, biogeochemically important tracers that have strong vertical gradients in the upper ocean (e.g., dissolved oxygen [*Emerson*, 1987] or nitrate [*McClain et al.*, 1996]).

The results of this study are overall consistent with the concept that anomalous oceanic fluxes in the southern GOA are responsible for frequent perturbations from the typical annual cycle at durations from a month to a year or more. This has been inferred through comparison between surface inputs and oceanic storage of heat and freshwater during the Weathership era at OSP [*Tabata*, 1965; *Large*, 1996] and in the Gulf of Alaska during the Argo sampling period (2003-on) [*Jackson et al.*, 2006], or from changes in the pycnocline,

away from direct surface forcing, along Line P [*Crawford et al.*, 2007]. Here, the details of these oceanic fluxes could also be estimated due to persistent, depth-resolved sampling of spatial gradients at OSP.

4.2. Vertical Velocity and Diffusivity

Vertical velocity and diffusivity estimated by the least-squares solution are in accord with the magnitude and vertical structure expected based on previous studies. For w, estimates in the GOA have relied on theoretical calculations based on wind-stress curl, numerical modeling results, or inferential approaches similar to this study. As an example, the steady-state least-squares problem described by *Matear* [1993], which has many similarities to this study, estimated $w \approx 0.4$ m d^{-1} in the lower halocline, the upper boundary of the domain considered by *Matear* [1993]. This is larger than the mean value in this study, but within the range of monthly variability. Recently, *Freeland* [2013a] used the Argo array to estimate upwelling at 700 dbar averaged across the central Gulf of Alaska that ranged from 0.02 to 0.12 m d^{-1} from 2003 to 2010, similar to the mean upwelling in the upper pycnocline estimated here. Other studies focusing on upwelling in the main pycnocline indicate net positive w and steady state values between 0.003 and 0.4 m d^{-1} [*Tabata*, 1965; *Duce*, 1986; *Roden*, 1991; *de Baar et al.*, 1995; *Matear and Wong*, 1997], with monthly variability due to wind stress curl as large as $\mathcal{O}(1)$ m d^{-1} [*Tabata*, 1965; *McClain et al.*, 1996; *Cummins and Lagerloef*, 2002] and upwelling induced by isopycnal rebound within anticyclonic eddies up to 0.7 m d^{-1} [*Johnson et al.*, 2005; *Nudds and Shore*, 2011].

Monthly variability in the estimated upwelling during Seaglider surveys is partially explained by Ekman pumping, but with greater-than-expected amplitude and significant residuals. One possible mechanism accounting for the residuals is the forcing of vertical motion by mesoscale variability [*Wang and Ikeda*, 1997; *Shearman et al.*, 1999], associated in this instance with the meander illustrated in PEC1. Unfortunately, this possibility cannot be quantitatively evaluated using, e.g., the quasi-geostrophic omega equation, because this method requires second-order horizontal derivatives of density, which are not resolved by Seaglider surveys at OSP [*Pelland*, 2015].

Vertical eddy diffusivity estimated by the least-squares problem was resolved well in the upper TL, where it was estimated to play a dominant role in the vertical redistribution of heat and salt throughout the annual cycle. Eddy diffusivity was consistently elevated at the base of the SL by up to 2 orders of magnitude relative to interior values, and decreased rapidly to the depth of maximum stratification. This is in excellent agreement with microstructure measurements that span the upper-ocean boundary layer (e.g., *Raymond et al.*, [2004], their Figure 10; *Lozovatsky et al.* [2006], their Figure 7; *Sun et al.* [2013], their Figures 4, 6, and 9; *Fernández-Castro et al.* [2014], their Figure 10). In this study, the rate of decrease with depth also showed seasonal differences, which are not explored further but are possibly related to seasonal differences in energy input or stratification in the upper TL [*Grant and Belcher*, 2011].

The monthly intervals in which turbulent flux is estimated in this study likely has the effect of vertically smoothing the estimated diffusivity, since the turbulent flux is cast as proportional to κ and the vertical gradients of a mean monthly vertical profile of each property. Profiles of κ determined over a shorter period would likely exhibit vertical transitions that are at least as sharp as those determined here. As an example, *Rousseau et al.* [2010] estimated vertical profiles of turbulent dissipation and diapycnal diffusivity from microstructure profiling at OSP during 7–11 June 2007. The mean profile of diapycnal diffusivity (roughly equivalent to the vertical diffusivity estimated in this study, given the nearly vertical gradient of density in the upper ocean) shown in their Figure 1 exhibits a rapid extinction with depth until reaching the depth of the maximum transition layer stratification at 60 m. The rate of decrease is approximately four decades over 25 m, nearly twice that observed in this study.

Seasonal variability was also evident in diffusivity profile amplitude in this study, consistent with the results of *Cronin et al.* [2015]. These authors found that climatological diffusivity at the SL base (defined differently than in this study) at OSP increased from $\sim$1 $\times$10^{-4} m^2 s^{-1} in summer to $\sim$3 $\times$10^{-4} m^2 s^{-1} in the fall. The estimated increase in diffusivity from June–August to October–December during Seaglider surveys is broadly consistent with the *Cronin et al.* [2015] results, albeit with a weaker seasonal amplitude.

The summer and fall values of heat flux at the SL base are in good agreement between this study and *Cronin et al.* [2015], with values <100 W m^{-2} of downward flux in summer increasing to $\sim$100 W m^{-2} or greater in September–November. Like this study, the *Cronin et al.* [2015] climatological downward heat

fluxes at the base of the SL in December–February are estimated to be weaker than those in the fall, though the amplitude of the seasonal variations in heat flux are much larger here. Results are also consistent in that the turbulent flux of heat dominates the turbulent buoyancy flux at the SL base except during winter and early spring.

The greatest disagreement between the *Cronin et al.* [2015] results and those of this study is in April, where their climatology shows the largest turbulent heat flux and diffusivity at the base of the SL, in contrast to weak heat flux and diffusivity estimated here. In both analyses, the uncertainties are largest during this month (cf., confidence bounds on κ in Figure 9). The effects of turbulence in the transition layer during the restratification period warrant further observation given the importance of this period to annual balances of biogeochemical tracers in the SL [*Fassbender et al.*, 2016].

4.3. Model Validity

In any least-squares problem, assessing the validity of the assumptions underlying the governing system of equations is as important as determining the confidence bounds on elements of the solution [*Wunsch*, 1978]. In this study, the governing tracer equations contain two important simplifications that arise from limitations inherent to the Seaglider-mooring array deployed at OSP. First, the variables that compose the balances (1)-(2) are assumed constant within each month. This time scale was chosen out of necessity in order to match the time scale of the least-squares problem with the time required for Seagliders to effectively survey the spatial domain surrounding the OSP mooring. This assumption smears over many storms and abrupt changes in SL temperature or thickness that occur on time scales of 1–2 days [e.g., *Davis et al.*, 1981b; *Large et al.*, 1986; *Paduan and deSzoeke*, 1986; *Large and Crawford*, 1995; *Dohan and Davis*, 2011]. Horizontal diffusion is also omitted, despite evidence of thermohaline fine structure in the halocline characteristic of horizontal interleaving and, potentially, fine-scale cross-frontal heat and salt transport (PEC1). This was done primarily because, in order to estimate convergence or divergence of cross-frontal transport, it is necessary to compute the horizontal curvatures of θ and S, which are not resolved by Seaglider surveys as noted above.

The validity of a least-squares solution that includes the above simplifications can be assessed by weighing the ability of the solution to account for real variability in the observed tracer fields, while also estimating realistic velocity and diffusivity components [*Olbers et al.*, 1985]. The results described here are in these respects encouraging. Although the maximum solution residuals in each tracer balance were large, these were much reduced when averaging over time or depth. At individual depth levels, the time-mean square residual in the temperature and salinity records predicted by the solution vector was on average $\sim$20% of the variance, consistent with the problem construction. When averaging over distinct vertical layers the solution temperature and salinity accurately describes seasonal variability in the upper ocean and secular variability in the halocline, while reproducing the observed bulk vertical thermal and haline stratification at OSP in all months but one. The solution achieves this level of accuracy without excessive departure of the solution elements (u, v, w, κ) from a priori information or general expectations, suggesting that they are not unduly compensating for the effect of omitted terms. Overall, these properties support the idea that the terms contained in (1) and (2) are sufficient to account for bulk variations in heat and salt content at monthly time scales at OSP.

As noted by *Wunsch* [1978, 1996], the governing equations can never be proven to be correct to the exclusion of all other possibilities, but merely consistent with the observed data. Other solutions obtained during the development of this study indicate that the conclusions are not particularly sensitive to alternate combinations of physically realistic assumptions, at least within a limited range. *Pelland* [2015] found that a similar least-squares problem that included horizontal advection due to specified, monthly average horizontal Ekman flows in the vector $\vec{b}$ in (9) produced comparable results, reducing the residuals in some tracer equations while increasing them in others. A formulation in which the Ekman flows were implicitly included in the solution $\vec{x}$, and the constraint (7) on $w(z=-H_j^{Ek})$ was omitted, also had comparable skill in explaining the observed variability (thickness-weighted NMSR of 0.191 for potential temperature, 0.215 for salinity, cf., section 3.1); the properties of the vertical velocity, diffusivity, and character of the balances in this solution were negligibly different from those described here. Ultimately, a solution without horizontal Ekman flows was preferred because it reduced the model complexity without significantly worsening the fit to the data.

The results are sensitive to altering the manner in which horizontal geostrophic advection is included in the problem, or whether it is included at all, though in ways that support the assumptions and conclusions of this study. *Pelland* [2015] found that formulating the problem with governing equations that excluded horizontal advection entirely had poorer ability to explain the observed variability, especially deeper than 80 m, indicating that horizontal advection must be invoked to explain the observed changes there. On the other hand, assuming that the horizontal currents $\vec{u}^g$ estimated in PEC1 and the resulting advection were known with small error such that they could be moved to the vector $\vec{b}$ also gave large residuals [*Pelland*, 2015]. This supports the choice to include u and v as unknowns in this problem.

5. Conclusions

While tracer balances at OSP are often approximated for short periods as being dominated by vertical fluxes and local storage, seasonal and transient horizontal advection of heat and salt are in fact important. This study demonstrates that this advection can take different forms in different years, and can have varying impacts in different vertical layers of the upper ocean. A complete diagnosis of the monthly balances of heat and salt during Seaglider surveys at OSP would not have been possible without information regarding horizontal spatial gradients. Autonomous vehicle surveys provide one strategy for persistently sampling these gradients at OSP and other time series sites.

Horizontal gradients measured by these surveys also allowed for inference of unmeasured vertical velocity and depth-resolved eddy diffusivity in the upper ocean over more than one annual cycle, which had not been previously achieved from observations at OSP. These quantities play a critical role in the vertical exchange of physical tracers, nutrients, and dissolved gases between the well-mixed surface layer and stratified interior. Results of this study emphasize that vertical velocity and diffusivity exhibit meaningful variations with time and, for diffusivity, with depth in the stratified upper ocean. Accounting for these variations in a realistic manner is likely to be important for the accurate diagnosis of the balances of biogeochemical tracers and isolation of the effects of net biological productivity, respiration, or calcification [e.g., *Bushinsky and Emerson*, 2015; *Fassbender et al.*, 2016].

Continued observational monitoring of advective and diffusive transports at OSP is critical for further understanding of tracer balances there, especially in light of recent interannual anomalies in sea surface temperature [*Whitney*, 2015; *Bond et al.*, 2015], and evidence of long-term trends in stratification, alterations to the annual cycle of surface mixing, and consequent possible changes in the availability of nutrients to the surface ocean at OSP [*Freeland et al.*, 1997; *Freeland and Cummins*, 2005; *Li et al.*, 2005; *Jackson et al.*, 2009; *Freeland*, 2013b, though see *Thomson and Fine*, 2009]. We note that there has as yet been no large-scale, systematic attempt to test the conceptual annual cycle described in section 1, or investigate the detailed phenomenology of the recent warm anomaly, by closing the heat and salt balances including the effects of advection using observations in the GOA over several years. At OSP, the ongoing glider-moored observations as part of the National Science Foundation-supported Ocean Observatories Initiative (OOI) array could potentially extend the results of this study by resolving heat, freshwater, and other tracer balances at finer temporal scales. Results here and in PEC1 indicate that future autonomous measurements at OSP should concentrate on accurate and higher-frequency measurement of horizontal gradients and, if possible, independent measurement of vertical turbulent flux in order to more fully constrain the upper-ocean heat and salt balances over the annual cycle. If deployed for a sufficient period of time this array may be able to offer insight regarding outstanding questions in the southern GOA such as the role of high-frequency advection, mechanisms accounting for vertical motion in the main pycnocline, the nature of climatological seasonal cooling, and processes in the surface boundary layer during the restratification period.

Appendix A: Surface Fluxes Details and Remote Sensing Data

Latent and sensible heat fluxes were computed from NOAA OCS buoy data using the Coupled Ocean-Atmosphere Response Experiment (COARE) 3.0 algorithm [*Fairall et al.*, 2003] with warm layer and cool-skin corrections, while net solar and longwave radiation were estimated using the measured downwelling values and a seasonal cycle for surface albedo based on the ISCCP project [*Zhang et al.*, 2004]. Rain gauge measurements were corrected for wind effects following *Serra et al.* [2001], while evaporation was estimated using estimated latent heat flux and buoy-measured sea surface temperature.

During Seaglider surveys at OSP, a mooring line failure occurred on 11 November 2008, and mooring surface fluxes were unavailable from that date until redeployment on 14 June 2009. During this and any other gaps in surface fluxes due to buoy hardware failures, daily-average latent and sensible heat fluxes were obtained from the OAFLUX data set [*Yu and Weller*, 2007]. Data provided by ISCCP, also hosted at the OAFLUX website, were used to estimate surface radiative fluxes. These data were provided on a 1° grid at daily resolution.

Corrections were applied to two components of the OAFLUX/ISCCP surface heat fluxes to improve agreement with the moored time series, under the reasoning that the in situ sampling of the mooring is less likely to be biased, and to ensure consistency in the surface flux products that were used in the least-squares problem. Comparison of the ISCCP estimates of net upward longwave radiative flux to daily-average OCS buoy-based measurements during periods of overlap in 2007–2009 indicated a bias of -11.0 ± 6.5 W m^{-2} (ISCCP minus buoy). This bias was removed prior to application of the product to this study. The 2007–2009 overlap period used to evaluate this bias corresponds to the availability of ISCCP data, and the confidence interval is 95% based on a Student's t distribution with 24 degrees of freedom, which is the number of months of continuous data coverage overlap between ISCCP and OCS mooring. This is a conservative number of degrees of freedom, since daily longwave fluxes in the ISCCP product were found to have an e-folding decorrelation time scale of a few days (data not shown).

Similarly, OAFLUX sensible heat flux estimates were found to have a bias of -6.4 ± 2.6 W m^{-2} relative to buoy-based estimates. Latent heat fluxes from OAFLUX and ISCCP net shortwave radiation were not found to have significant biases within the period of overlap with the OCS buoy, and these components of the net surface heat flux were not corrected. After removal of the above biases, the resulting monthly average net heat flux from OAFLUX + ISCCP had a bias relative to the buoy of 0.8 W m^{-2} and RMS difference of 18.3 W m^{-2} during periods of overlap. By comparison, RMS monthly average net surface heat flux measured from the mooring was 108 W m^{-2} during the period 2007–2009.

Net moisture flux during mooring absence was estimated as the difference between OAFLUX net surface evaporation and GPCP 1DD V1.2 daily precipitation estimates [*Huffman et al.*, 2001]. Similar to the heat flux components as described above, monthly average precipitation estimates from the GPCP product were compared to those of the OCS mooring during periods of overlap between the instruments in the years 2007–2013. The period of comparison was extended beyond the glider survey period in order to increase the amount of overlap between the instruments and reliability of the bias estimate, assuming that the bias is constant through time. Here, monthly rather than daily averages were compared due to the large number of zero values in precipitation data. The monthly average GPCP estimates of precipitation P_{GPCP} were found to generally overestimate the precipitation relative to the mooring. Estimates of P_{GPCP} (units of cm d^{-1}) were corrected according to

$$P_{\text{GPCP,cor}} = 0.6643 P_{\text{GPCP}} + 0.0375, \tag{A1}$$

which was determined from a linear least-squares fit to mooring monthly average P versus P_{GPCP}. Similarly, OAFLUX evaporation E_{OA} (cm d^{-1}) was corrected according to

$$E_{\text{OA,cor}} = 1.0125 E_{\text{OA}} - 0.0168. \tag{A2}$$

Following these adjustments, the RMS disagreement between monthly average evaporation E minus precipitation P estimated from the OCS mooring and from the OAFLUX and GPCP products was 0.077 cm d^{-1}. By comparison, RMS monthly average net moisture flux measured from the mooring was 0.156 cm d^{-1} during 2007–2009.

Appendix B: Solution Diagnostics

The "Problem LSI/LDP" algorithm [*Lawson and Hanson*, 1974] used to solve the system (9) subject to the constraints (10) involves computing the singular value decomposition of the matrix $\mathbf{G} = \mathbf{W}^{1/2}\mathbf{A}$:

$$\mathbf{G} = \mathbf{U}\mathbf{S}\mathbf{V}^{\text{T}}, \tag{B1}$$

where $\mathbf{U}$ and $\mathbf{V}$ are orthogonal matrices, respectively, describing the column and row space of $\mathbf{G}$, and $\mathbf{S}$ is a diagonal matrix of singular values. The spectrum of singular values obtained from (B1), ordered by decreasing value, is shown in Figure B1a. This spectrum is a useful diagnostic of the properties of matrix $\mathbf{G}$ because,
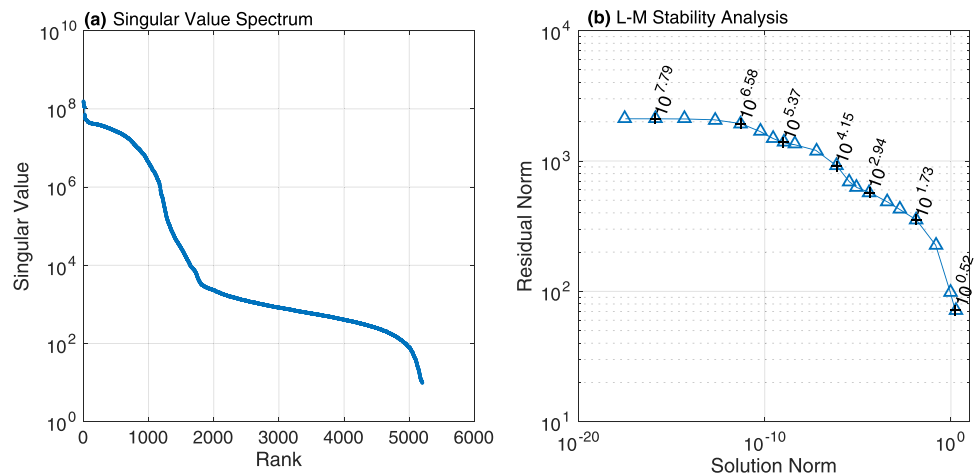
Figure B1. (a) Spectrum of singular values for the system of equations (9). (b) Residual norm versus solution norm in a Levenberg-Marquardt (L-M) analysis of the system (9), evaluated using several values of the L-M parameter λ_c. Each triangle represents a result obtained with a different λ_c value. These values are labeled for selected points. λ_c varies from the largest singular value (top left-most point) to 1/3 of the smallest singular value (bottom right-most) [*Zhang and Hogg*, 1992].

if this matrix were not full rank, the singular value spectrum would exhibit an abrupt drop off beyond the smallest resolved singular value [e.g., *Anokhin et al.*, 2008, their Figure 9]. Singular values smaller than such a drop off contribute significantly to the amplitude of the solution, but draw their information primarily from noise in the input data [*Olbers et al.*, 1985]. However, the absence of any abrupt drop off in the spectrum of Figure B1a suggests that the matrix **G** is of full rank and that all singular values are well-resolved [*Hogg*, 1987; *Zhang and Hogg*, 1992].

An additional useful diagnostic of the system (9) is a Levenberg-Marquardt (L-M) stability analysis, results of which are shown in Figure B1b. This analysis assesses the sensitivity of the residual norm and solution norm to the L-M cutoff parameter λ_c, where singular values comparable to or smaller than the given λ_c are filtered out of the solution [*Zhang and Hogg*, 1992; *Hautala and Riser*, 1993; *Anokhin et al.*, 2008; *Lawson and Hanson*, 1974, pp. 190–198]. Hence, as λ_c increases in size, only the lowest modes (greatest singular values) of the solution are retained. In the case that **G** is not full rank, as λ_c decreases below the level of the smallest significant singular value, the norm of the solution vector increases without any corresponding benefit in decrease of the residual norm [e.g., *Lawson and Hanson*, 1974, their Figure 26.2]. However, such a plateau in the L-M diagram is not apparent in Figure B1b. Based on these diagnostics, we conclude that **G** is of full rank, and the solution was obtained using Problem LSI/LDP while retaining all singular values in (B1).

The parameter resolution ($\mathbf{VV}^\mathsf{T}$) and data resolution ($\mathbf{UU}^\mathsf{T}$) matrices (not shown) were approximately diagonal with all diagonal elements > 0.99. This indicates that the solution parameters are independently resolved and all equations contribute information to the solution, respectively [*Wiggins*, 1972; *Wunsch*, 1978]. The covariance matrix for errors on the vector $\vec{x}$ of the solution elements, $\langle \delta\vec{x}\,\delta\vec{x}^\mathsf{T}\rangle$, was estimated as [*Zhang and Hogg*, 1992; *Lawson and Hanson*, 1974, pp. 67–68]

$$\langle \delta\vec{x}\,\delta\vec{x}^\mathsf{T}\rangle = \frac{\vec{\epsilon}^\mathsf{T}\vec{\epsilon}}{m-n}\left(\mathbf{V}\mathbf{S}^{-2}\mathbf{V}^\mathsf{T}\right) \tag{B2}$$

where m and n are, respectively, the number of rows and columns of **A**. The vector of confidence bounds on the solution elements was then estimated as $t_{\mathrm{CDF}}^{-1}(0.975, m-n)\sqrt{\mathrm{diag}\left(\langle \delta\vec{x}\,\delta\vec{x}^\mathsf{T}\rangle\right)}$, where $t_{\mathrm{CDF}}^{-1}(p, \nu)$ is the inverse Student's t cumulative distribution evaluated at probability p and with degrees of freedom ν [*Hautala and Riser*, 1993; *Anokhin et al.*, 2008].

References

Anokhin, V., J. Imberger, G. Ivey, and J. Romero (2008), Estimating net transport and mixing using a time-dependent inverse method, *J. Geophys. Res.*, *113*, C07006, doi:10.1029/2006JC003705.

Beaird, N. L., I. Fer, P. B. Rhines, and C. C. Eriksen (2012), Dissipation of turbulent kinetic energy inferred from Seagliders: An application to the Eastern Nordic seas overflows, *J. Phys. Oceanogr.*, 42, 2268–2282.

Bond, N., M. Cronin, H. Freeland, and N. Mantua (2015), Causes and impacts of the 2014 warm anomaly in the NE Pacific, *Geophys. Res. Lett.*, 42, 3414–3420doi:10.1002/2015GL063306.

Boyer, T., et al. (2013), World ocean database 2013, in *NOAA Atlas NESDIS 72*, edited by S. Levitus and A. Mishonov, 209 pp., NOAA Natl. Oceanogr. Data Cent., Silver Spring, Md. [Available at http://doi.org/10.7289/V5NZ85MT.]

Bushinsky, S. M., and S. Emerson (2015), Marine biological production from in situ oxygen measurements on a profiling float in the subarctic Pacific Ocean, *Global Biogeochem. Cycles*, 29, 2050–2060, doi:10.1002/2015GB005251.

Cleveland, W. S., and S. J. Devlin (1988), Locally weighted regression: An approach to regression analysis by local fitting, *J. Am. Stat. Assoc.*, 83(403), 596–610.

Crawford, W., J. Galbraith, and N. Bolingbroke (2007), Line P ocean temperature and salinity, 1956–2005, *Prog. Oceanogr.*, 75, 161–178.

Cronin, M., N. Bond, J. Farrar, H. Ichikawa, S. Jayne, Y. Kawai, M. Konda, B. Qiu, L. Rainville, and H. Tomita (2013), Formation and erosion of the seasonal thermocline in the Kuroshio Extension Recirculation Gyre, *Deep Sea Res., Part II*, 85, 62–74.

Cronin, M. F., and T. Tozuka (2016), Steady state ocean response to wind forcing in extratropical frontal regions, *Sci. Rep.*, 6, 28842, doi:10.1038/srep28842.

Cronin, M. F., N. Pelland, W. Crawford, and S. Emerson (2015), Estimating diffusivity from the mixed layer heat and salt balances in the North Pacific, *J. Geophys. Res. Oceans*, 120, 7346–7362, doi:10.1002/2015JC011010.

Cummins, P., and G. Lagerloef (2002), Low-frequency pycnocline depth variability at ocean weather station P in the Northeast Pacific, *J. Phys. Oceanogr.*, 32, 3207–3215.

Davis, R., R. deSzoeke, D. Halpern, and P. Niiler (1981a), Variability in the upper ocean during MILE: Part I: The heat and momentum balances, *Deep Sea Res., Part A*, 28(12), 1427–1451.

Davis, R., R. deSzoeke, and P. Niiler (1981b), Variability in the upper ocean during MILE: Part II: Modeling the mixed layer response, *Deep Sea Res., Part A*, 28, 1453–1475.

de Baar, H. J. W., J. T. M. de Jong, D. C. E. Bakker, B. M. Löscher, C. Veth, U. Bathmann, and V. Smetacek (1995), Importance of iron for plankton blooms and carbon dioxide drawdown in the Southern Ocean, *Nature*, 373, 412–415.

Denman, K., and M. Miyake (1973), Upper layer modification at ocean station Papa: Observations and simulation, *J. Phys. Oceanogr.*, 3(2), 185–196.

Dohan, K., and R. Davis (2011), Mixing in the transition layer during two storm events, *J. Phys. Oceanogr.*, 41, 42–66.

Duce, R. A. (1986), The impact of atmospheric nitrogen, phosphorus, and iron species on marine biological productivity, in *The Role of Air-sea Exchange in Geochemical Cycling*, edited by P. Buat-Ménard, pp. 497–529, Reidel Publ. Co., Dordrecht, Netherlands.

Emerson, S. (1987), Seasonal oxygen cycles and biological new production in surface waters of the subarctic Pacific Ocean, *J. Geophys. Res.*, 92(C6), 6535–6544.

Eriksen, C., T. Osse, R. Light, T. Wen, T. Lehman, P. Sabin, J. Ballard, and A. Chiodi (2001), Seaglider: A long-range autonomous underwater vehicle for oceanographic research, *IEEE J. Oceanic Eng.*, 26(4), 424–436.

Fairall, C., E. Bradley, J. Hare, A. Grachev, and J. Edson (2003), Bulk parameterization of air-sea fluxes: Updates and verification for the COARE algorithm, *J. Clim.*, 16, 571–591.

Fassbender, A., C. Sabine, and M. Cronin (2016), Net community production and calcification from seven years of NOAA Station Papa mooring measurements, *Global Biogeochem. Cycles*, 30, 250–267, doi:10.1002/2015GB005205.

Fernández-Castro, B., B. Mouriño Carballido, V. Benítez-Barrio, P. Chouciño, E. Fraile-Nuez, R. Graña, M. Piedeleu, and A. Rodríguez-Santana (2014), Microstructure turbulence and diffusivity parameterization in the tropical and subtropical Atlantic, Pacific and Indian Oceans during the Malaspina 2010 expedition, *Deep Sea Res., Part I*, 94, 15–30.

Frajka-Williams, E., C. C. Eriksen, P. B. Rhines, and R. R. Harcourt (2011), Determining vertical water velocities from Seaglider, *J. Atmos. Oceanic Technol.*, 28, 1641–1656.

Freeland, H. (2013a), Vertical velocity estimates in the North Pacific using Argo floats, *Deep Sea Res., Part II*, 85, 75–80.

Freeland, H., and P. Cummins (2005), Argo: A new tool for environmental monitoring and assessment of the world's oceans, an example from the N.E. Pacific, *Prog. Oceanogr.*, 64, 31–44.

Freeland, H., K. Denman, C. Wong, F. Whitney, and R. Jacques (1997), Evidence of change in the winter mixed layer in the Northeast Pacific Ocean, *Deep Sea Res., Part I*, 44(12), 2117–2129.

Freeland, H. J. (2013b), Evidence of change in the winter mixed layer in the Northeast Pacific Ocean: A problem revisited, *Atmos. Ocean*, 51(1), 126–133.

Gill, A., and P. Niiler (1973), The theory of the seasonal variability in the ocean, *Deep Sea Res. Oceanogr. Abstr.*, 20, 141–177.

Grant, A., and S. Belcher (2011), Wind-driven mixing below the oceanic mixed layer, *J. Phys. Oceanogr.*, 41, 1556–1575.

Hautala, S. L., and S. C. Riser (1993), A nonconservative β-spiral determination of the deep circulation in the Eastern South Pacific, *J. Phys. Oceanogr.*, 23, 1975–2000.

Hogg, N. (1987), A least-squares fit of the advective-diffusive equations to Levitus Atlas data, *J. Mar. Res.*, 45, 347–375.

Huffman, G., R. Adler, M. Morrissey, D. Bolvin, S. Curtis, R. Joyce, B. McGavock, and J. Susskind (2001), Global precipitation at one-degree daily resolution from multisatellite observations, *J. Hydrometeorol.*, 2(1), 36–50.

Jackson, J. M., P. G. Myers, and D. Ianson (2006), An examination of advection in the northeast Pacific Ocean, 2001–2005, *Geophys. Res. Lett.*, 33, L15601, doi:10.1029/2006GL026278.

Jackson, J. M., P. G. Myers, and D. Ianson (2009), An examination of mixed layer sensitivity in the northeast pacific ocean from July 2001-July 2005 using the general ocean turbulence model and argo data, *Atmos. Ocean*, 47(2), 139–153.

Johnson, W. K., L. A. Miller, N. E. Sutherland, and C. S. Wong (2005), Iron transport by mesoscale Haida eddies in the Gulf of Alaska, *Deep Sea Res., Part II*, 52, 933–953.

Kubota, M., N. Iwabe, M. Cronin, and H. Tomita (2008), Surface heat fluxes from the NCEP/NCAR and NCEP/DOE reanalyses at the Kuroshio Extension Observatory buoy site, *J. Geophys. Res.*, 113, C02009, doi:10.1029/2007JC004338.

Large, W. G. (1996), An observational and numerical investigation of the climatological heat and salt balances at OWS Papa, *J. Clim.*, 9, 1856–1876.

Large, W. G., and G. B. Crawford (1995), Observations and simulations of upper-ocean response to wind events during the ocean storms experiment, *J. Phys. Oceanogr.*, 25, 2831–2852.

Large, W. G., J. C. McWilliams, and P. P. Niiler (1986), Upper ocean thermal response to strong autumnal forcing of the Northeast Pacific, *J. Phys. Oceanogr.*, 16, 1524–1550.

Large, W. G., J. C. McWilliams, and S. Doney (1994), Oceanic vertical mixing: A review and a model with a nonlocal boundary layer parameterization, *Rev. Geophys.*, 32(4), 363–403.

Lawson, C., and R. Hanson (1974), *Solving Least Squares Problems*, 340 pp., Prentice-Hall, Englewood Cliffs, N. J.

Ledwell, J. R., A. J. Watson, and C. S. Law (1993), Evidence for slow mixing across the pycnocline from an open-ocean tracer-release experiment, *Nature*, *364*(6439), 701–703.

LeVeque, R. (2007), Finite Difference Methods for Ordinary and Partial Differential Equations, Steady State and Time Dependent Problems, 341 pp., Soc. for Ind. and Appl. Math., Philadelphia, Pa.

Li, M., P. Myers, and H. Freeland (2005), An examination of historical mixed layer depths along Line P in the Gulf of Alaska, *Geophys. Res. Lett.*, *32*, L05613, doi:10.1029/2004GL021911.

Lozovatsky, I. D., E. Roget, H. J. S. Fernando, M. Figueroa, and S. Shapovalov (2006), Sheared turbulence in a weakly stratified upper ocean, *Deep Sea Res., Part I*, *53*, 387–407.

Matear, R. J. (1993), Circulation within the ocean storms area located in the Northeast Pacific ocean determined by inverse methods, *J. Phys. Oceanogr.*, *23*, 648–658.

Matear, R. J., and C. S. Wong (1997), Estimation of vertical mixing in the upper ocean at Station P from chlorofluorocarbons, *J. Mar. Res.*, *55*(3), 507–521.

McClain, C., K. Arrigo, K.-S. Tai, and D. Turk (1996), Observations and simulations of physical and biological processes at ocean weather station P, 1951–1980, *J. Geophys. Res.*, *101*(C2), 3697–3713.

McDougall, T. (1984), The relative roles of diapycnal and isopycnal mixing on subsurface water mass conversion, *J. Phys. Oceanogr.*, *14*(10), 1577–1589.

Moisan, J. R., and P. P. Niiler (1998), The seasonal heat budget of the North Pacific: Net heat flux and heat storage rates (1950–1990), *J. Phys. Oceanogr.*, *28*, 401–421.

Nudds, S., and J. Shore (2011), Simulated eddy induced vertical velocities in a Gulf of Alaska model, *Deep Sea Res., Part I*, *58*, 1060–1068.

Olbers, D., M. Wenzel, and J. Willebrand (1985), The inference of North Atlantic circulation patterns from climatological hydrographic data, *Rev. Geophys.*, *23*(4), 313–356.

Paduan, J., and R. deSzoeke (1986), Heat and energy balances in the upper ocean at 50°N, 140°W during November 1980 (STREX), *J. Phys. Oceanogr.*, *16*, 25–38.

Paduan, J., and P. Niiler (1993), Structure of velocity and temperature in the Northeast Pacific as measured with Lagrangian Drifters in Fall 1987, *J. Phys. Oceanogr.*, *23*, 585–600.

Paulson, C., and J. Simpson (1977), Irradiance measurements in the Upper Ocean, *J. Phys. Oceanogr.*, *7*, 952–956.

Pelland, N. (2015), Eddy circulation, heat and salt balances, and ocean metabolism: Observations from a Seaglider-mooring array at ocean station Papa, PhD thesis, Univ. of Wash., Seattle. [Available at http://hdl.handle.net/1773/35285.]

Pelland, N. A., C. C. Eriksen, and M. F. Cronin (2016), Seaglider surveys at Ocean Station Papa: Circulation and water mass properties in a meander of the North Pacific current, *J. Geophys. Res. Oceans*, *121*, 6816–6846, doi:10.1002/2016JC011920.

Raymond, D., S. Esbensen, C. Paulson, M. Gregg, C. Bretherton, W. Petersen, and R. Cifelli (2004), EPIC2001 and the coupled ocean-atmosphere system of the tropical East Pacific, *Bull. Am. Meteorol. Soc.*, *85*, 1341–1354.

Ren, L., and S. Riser (2009), Seasonal salt budget in the northeast Pacific Ocean, *J. Geophys. Res.*, *114*, C12004, doi:10.1029/2009JC005307.

Rhines, P. (1986), Vorticity dynamics of the oceanic general circulation, *Annu. Rev. Fluid Mech. 18*, 433–497.

Ridgway, K. R., J. R. Dunn, and J. L. Wilkin (2002), Ocean interpolation by four-dimensional weighted least squares–application to the waters around Australasia, *J. Atmos. Oceanic Technol.*, *19*, 1357–1376.

Roden, G. (1991), Subarctic-subtropical transition zone of the North Pacific: Large-scale aspects and mesoscale structure, in *Biology, Oceanography, and Fisheries of the North Pacific Transition Zone and Subarctic Frontal Zone, NOAA Tech. Rep. NMFS 105*, pp. 1–38, NMFS Sci. Publ. Off., Seattle, Wash. [Available at http://spo.nwr.noaa.gov/tr105.pdf.]

Rousseau, S., E. Kunze, R. Dewey, K. Bartlett, and J. Dower (2010), On turbulence production by swimming marine organisms in the open ocean and coastal waters, *J. Phys. Oceanogr.*, *40*, 2107–2121.

Rudnick, D. (2003), Observations of momentum transfer in the upper ocean: Did Ekman get it right?, in *Near-Boundary Processes and Their Parameterization, Proceedings of the 13th 'Aha Huliko'a Hawaiian Winter Workshop*, edited by P. Müller and D. Henderson, pp. 163–170, Dep. of Oceanogr., Univ. of Hawaii, Honolulu. [Available at http://www.soest.hawaii.edu/PubServices/2003pdfs/Rudnick.pdf.]

Schanze, J., R. Schmitt, and L. Yu (2010), The global oceanic freshwater cycle: A state-of-the-art quantification, *J. Mar. Res.*, *68*, 569–595.

Serra, Y., P. A'Hearn, H. Freitag, and M. McPhaden (2001), ATLAS Self-siphoning rain gauge error estimates, *J. Atmos. Oceanic Technol.*, *18*, 1989–2002.

Shearman, R. K., J. A. Barth, and P. M. Kosro (1999), Diagnosis of the three-dimensional circulation associated with mesoscale motion in the California current, *J. Phys. Oceanogr.*, *29*, 651–670.

Sun, O. M., S. R. Jayne, K. L. Polzin, B. A. Rahter, and L. C. St. Laurent (2013), Scaling turbulent dissipation in the transition layer, *J. Phys. Oceanogr.*, *43*, 2475–2489.

Tabata, S. (1965), Variability of oceanic conditions at Station ''P'' in the Northeast Pacific Ocean, *Trans. R. Soc. Can.*, *4*, 367–478.

Thomson, R., and I. Fine (2009), A diagnostic model for mixed layer depth estimation with application to ocean station P in the Northeast Pacific, *J. Phys. Oceanogr.*, *39*, 1399–1415.

Torruella, A. (1995), The fall upper ocean heat balance in the Northeast Pacific, PhD thesis, Scripps Inst. of Oceanogr., Univ. of Calif.-San Diego, San Diego, Calif.

Tziperman, E., and A. Hecht (1988), Circulation in the eastern levantine basin determined by inverse methods, *J. Phys. Oceanogr.*, *18*, 506–518.

Wang, J., and M. Ikeda (1997), Diagnosing ocean unstable baroclinic waves and meanders using the quasigeostrophic equations and Q-vector method, *J. Phys. Oceanogr.*, *27*, 1158–1172.

Waterhouse, A. F., et al. (2014), Global patterns of diapycnal mixing from measurements of the turbulent dissipation rate, *J. Phys. Oceanogr.*, *44*(7), 1854–1872.

Whitney, F. (2015), Anomalous winter winds decreases 2014 transition zone productivity in the NE Pacific, *Geophys. Res. Lett.*, *42*, 428–431, doi:10.1002/2014GL062634.

Wiggins, R. A. (1972), The general linear inverse problem: Implications of surface waves and free oscillations for earth structure, *Rev. Geophys. Space Phys.*, *10*(1), 251–285.

Wunsch, C. (1978), The North Atlantic general circulation west of 50°W determined by inverse methods, *Rev. Geophys. Space Phys.*, *16*(4), 583–620.

Wunsch, C. (1996), *The Ocean Circulation Inverse Problem*, 442 pp., Cambridge Univ. Press, Cambridge, U. K.

Yu, L., and R. Weller (2007), Objectively analyzed air-sea heat fluxes for the global ice-free oceans (1981–2005), *Bull. Am. Meteorol. Soc.*, *88*(4), 527–539.

Zhang, H.-M., and N. G. Hogg (1992), Circulation and water mass balance in the Brazil Basin, *J. Mar. Res.*, *50*, 385–420.

Zhang, Y., W. Rossow, A. Lacis, V. Oinas, and M. Mishchenko (2004), Calculation of radiative fluxes from the surface to top of atmosphere based on ISCCP and other global data sets: Refinements of the radiative transfer model and the input data, *J. Geophys. Res.*, *109*, D19105, doi:10.1029/2003JD004457.